ANL/APS/TB-24

Diamond Monochromators for APS Undulator-A Beamlines

R.C. Blasdell, L. A. Assoufid, and D. M. Mills

TABLE OF CONTENTS

1.   INTRODUCTION

There has been considerable interest in the use of diamonds in high-heat-load monochromators (HHLMs) in the last several years.[1-7] The superb thermal and mechanical properties of single crystal diamonds serve to minimize distortions caused by a given thermal load, while the low x-ray absorption cross section reduces both the total power deposited in the crystal, as well as the peak (volumetric) power density. The primary obstacle for the widespread use of diamonds at present is a lack of ready availability of perfect single crystals of the desired size and orientation. Although it is possible to obtain near-perfect natural diamonds of the size and orientation required for use on an undulator beamline (the Darwin widths are a bit larger than desired and the crystals are just big enough to attach to a thermal heat sink), the selection process is generally one of trial and error. Near perfect synthetic diamonds can currently be obtained in the minimum necessary size (typically 4-5 mm on a side), albeit these are difficult to obtain and are in limited quantities.

A collaborative agreement has been made between the staff of the Advanced Photon Source (APS), the European Synchrotron Radiation Facility (ESRF), and the Super Photon Ring-8 GeV (SPring-8) to explore the use of diamonds as high-heat-load monochromators is on-going. One of the avenues of research is to push for improved perfection and size of synthetic diamonds. Sumitomo Electric Corporation of Japan has agreed to work with staff from SPring-8 to grow [100] oriented perfect single-crystal diamonds of $10 \times 10 \times 1$ mm^3 size by 1996/1997 (from which one could also cut pieces with the large face parallel to the (111) planes). They have taken the first step in producing an essentially perfect $4 \times 4 \times 1$ mm^3 type II diamond with less than 5 µrad (1 arc second) strain (measured over the entire surface).[8] We believe progress in the production of synthetic diamonds, as well as improvement in ties with suppliers of natural diamonds, should make available a relatively large number of high-quality diamonds of moderate size within the next several years.

Except at very low energies (< 3 keV), a diamond monochromator has a smaller energy bandpass than the equivalent silicon monochromator and so diamonds will probably not be every user's best friend. Nonetheless, one should be careful when making a comparison because it is still not known with certainty whether silicon-based designs will be able to endure the maximum heat loads of the APS and SPring-8 while providing beam on sample without a significant loss of spectral brilliance simply because x-ray beams of such combined spectral brilliance, power density, and total power do not exist yet. While people have been able to examine the throughput of HHLMs subject to high x-ray power loads, little work has been possible to ascertain whether the beam will retain its original phase space volume.[9,10]

Table 1.1[4-7,11] compares the essential results to date of the major high-heat-load experiments on diamond monochromators and the typical maximum heat loads that would be experienced by a diamond HHLM 30 m from an APS undulator A. The location of each experiment is given in column 2, the reference and year of publication are given in columns 1 and 3, the type and size of the diamond in columns 4 and 5, and the reflection geometry and cooling and mounting schemes in columns 6 and 7. The *absorbed* (rather than *incident*—there can be a considerable difference for diamond) total power and absorbed peak power density are given in columns 8 and 9. The calculated rocking curve widths (including dispersion), low-power and high-power rocking curve widths at the x-ray energy indicated in column 10 are given in columns 11-13. Two things are apparent from Table 1.1—first, no diamond monochromator has yet been subjected to the total power load expected at the APS, and, second, clearly measurable distortions are observed at the highest power loads experienced—about half that expected at the APS. (It is important to note that the principal problem for diamond HHLMs at the APS will be the total power deposited not the peak power density.) Not explicitly evident from Table 1.1 is the very

Table 1.1 Survey of diamond HHLM experiments. (See text for description of column headings.)

Year Publ.	Beamline	Refs.	Diamond Type	Size (mm³)	Geometry, Reflection	Cooling, Mounting	P_{abs} (W)	P_{abs} (W/mm²)	E (keV)	$\Delta\theta_0$ (μrad)	$\Delta\theta_{P=0}$ (μrad)	$\Delta\theta_{Pmax}$ (μrad)
1993	NSLS X25	5	S, ¹²C-IIa	4x4x0.5	B (4,0,0)	RW, GI	48	132*	22	16.0	19.4	27.5
1993	NSLS X25	6	S, ¹²C-IIa	4x4x0.5	B (4,0,0)	JW, CL	40	166*	22	-	12.6	17.5†
1993	ESRF ID6	7	N, -	0.25 thick	AL (1,1,1)	SW, CL?	4.4	1.1*	8	-	40	54†
1993	ESRF ID10	11	N, -	0.202 thick	AL (1,1,1)	SW, GI	<26?	<4?	9	22.1	35.6	34.1†
1994	ESRF BL3	4	S, Ib	4x8x0.109	SL (2,2,0)	SW, GI	8.7	109*	15	15.0	15.7	16.0†
Expected, APS UA			-	0.5 thick	B (1,1,1)	-	115	14	-	-	-	-
"			-	0.1 thick	AL (1,1,1)	-	50	7.5	-	-	-	-

* Absorbed peak power density estimated from ratio of absorbed to incident total power.

† Power level changed by masking the incident beam, so increased broadening in part due to increased field of view.

B = Bragg geometry

AL = Asymmetric Laue geometry

SL = Symmetric Laue geometry

RW = Rear indirect water cooled

JW = Jet direct water cooled

SW = Side indirect water cooled

CL = Clamped

GI = Floating on GaIn eutectic

S = Synthetic diamond

N = Natural diamond

¹²C = Isotopicaly pure (99.99% ¹²C) diamond.

2

encouraging information that the incident power and peak power density in the 1994 ESRF experiments at BL3 were 280 W and 3.4 kW/mm^2, respectively.[4]

The APS hands-on experience with the use of diamonds as high-heat-load monochromators has so far been rather limited. A water-jet-cooled diamond monochromator was tested on the APS/CHESS prototype undulator installed on CESR, the Cornell Electron-Position Storage Ring in the fall of 1993. A 6 x 6 x 0.3 mm^3, [100] oriented, type Ib Sumitomo (Sumicrystal$^®$) diamond was sealed to a jet-cooling apparatus with RTV silicone, a material known from past experiences to maintain resiliency and strength even when subjected to high doses of x-radiation. A symmetric Si (531) crystal was used as a near-dispersionless second crystal. With a 0.7 mm x 1.0 mm beam incident on the diamond, double-crystal rocking curves of less than 2.5 arc seconds were recorded at 15 keV (nearly independent of incident power from 0 to 15 watts), larger than the expected theoretical value of 0.8 arc seconds. When the beam size was increased to 2 mm x 3 mm and the stored beam current ramped to 100 mA, the RTV seal gave way under the pressure of the 0.1 MPa (15 psi) water jet. This was probably due to heating of the mount adjacent to the RTV seal by the transmitted x-ray beam resulting in a weakening of the RTV seal. Because of the limited time available for testing during the undulator run, these tests could not be pursued further.

In November of 1994, we had the opportunity to gain more experience when the APS staff participated in an experiment with the ESRF and SPring-8 to explore the performance of cryogenically cooled diamonds on the BL3 (focused wiggler) line at the ESRF. (The details of this experiment are discussed in Section 4.3 of this document.) In addition to the testing of diamonds on synchrotron sources, we have recently commissioned an in-house topography station that can be used to characterize diamond crystals, as well as other potential single-crystal optical components for users of the APS. One of the first such topographs taken with this instrument is shown in Figure 1.1

Simple theoretical calculations[1,3,12] (and experimental results) suggest that it should be possible to produce a diamond monochromator that can withstand the maximum expected heat load of APS Undulator (operating @ 7 GeV, 100 mA storage ring current) and provide approximately half the theoretical bandpass of a Si monochromator while preserving the brilliance of the beam (more details on the thermal calculations can be found in Chapter 4). Clearly diamonds look promising and already several CATs are seriously contemplating the use of a diamond monochromator as a first optical element on an APS undulator beamline. However, the needs of the twenty-odd insertion device beamlines planned for the initial startup of the APS vary considerably—for some diamond may be a good or expedient choice while for others it may not be. Likewise, beam multiplexing (so far accomplished with one Laue geometry crystal—others have yet to be installed) may be advantageous for a few diamond advocates while others will need a double Bragg geometry monochromator. Recognizing this diversity and the early stage of research on diamond monochromators, we do not advance a preferred design (or designs) for a monochromator at this time but instead attempt to provide a reference document that will allow designers not familiar with diamonds to more easily examine the possible advantages and disadvantages of diamond monochromators for their beamline(s). The APS is actively exploring possible diamond monochromator designs and is open to collaboration with CATs on the development of prototype monochromators, as well as general issues related to diamond quality and availability.

The first several sections of this document tabulate the general physical characteristics of diamond and diamond monochromators. This is followed by simple analytical and finite element analysis models of diamond monochromators and an overview of the APS R&D plans for diamond high-heat-load monochromators.
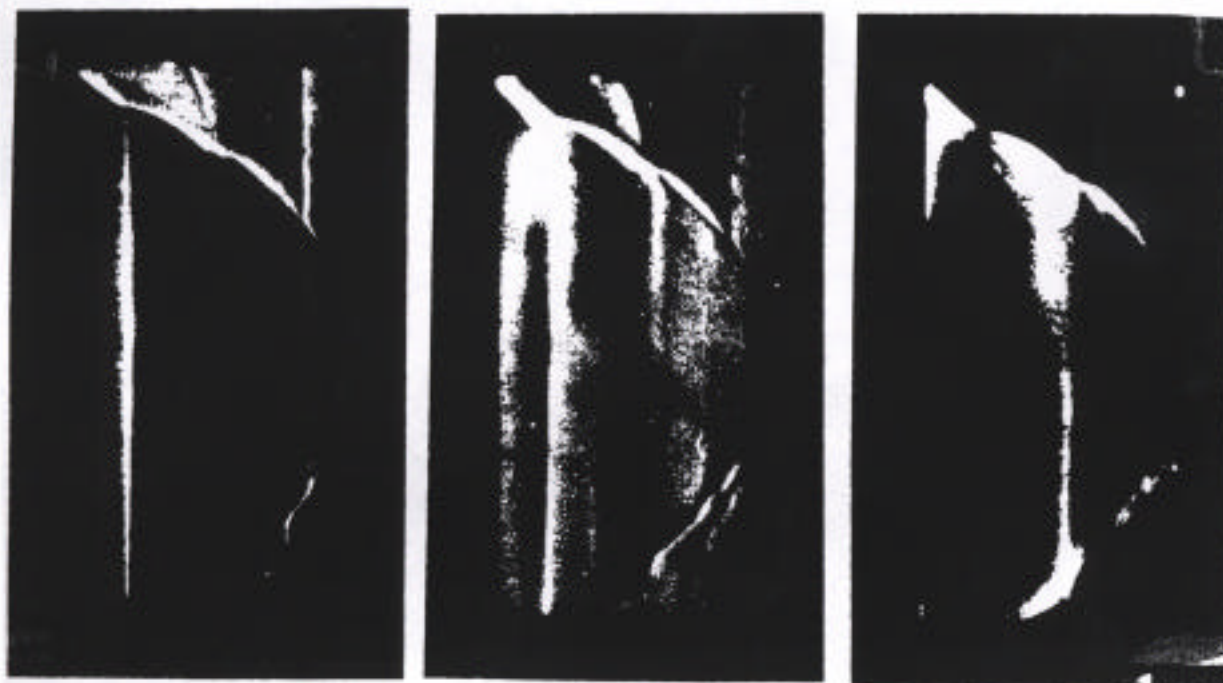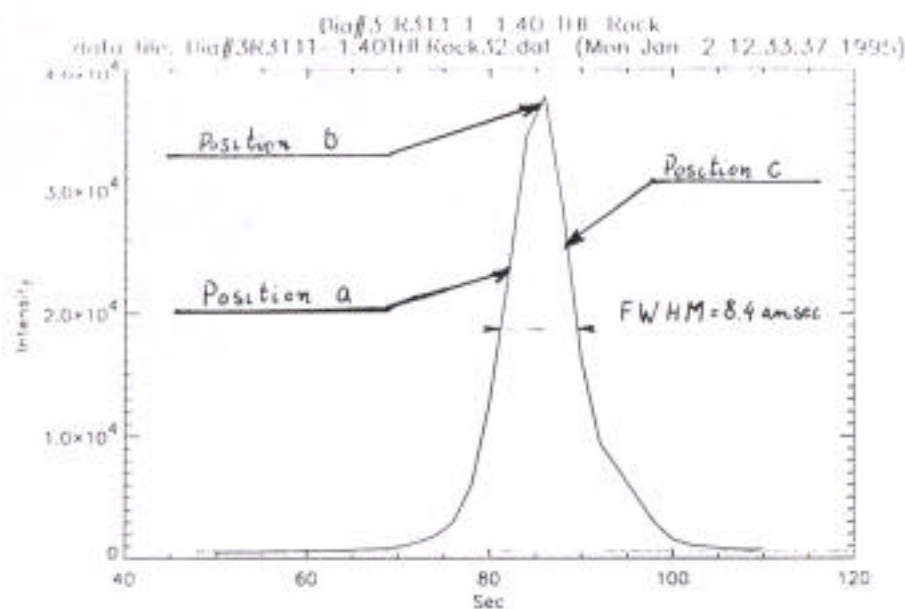
(a)   (b)   (c)

Figure 1.1 Double-crystal topograph of a [111] oriented synthetic diamond from Sumitomo. The diamond (311) reflection was used in the topograph taken with 8 keV radiadtion. An asymmetrically cut silicon (333) crystal served as the collimating monochromator. The size of the diamond was 3 mm x 7 mm. (Diamond courtesy of R. Hewitt, EXXON Corp., topograph taken by Felix Krasnicki, APS).

2.   PHYSICAL PROPERTIES OF DIAMONDS

2.1 Varieties of Diamonds

Diamonds come in a great variety of shapes and sizes, and in general may include substantial amounts of impurities (see, for example, refs. 13 and 14 for an extended discussion and additional references). Natural diamonds are produced in volcanic vent tubes and may include any impurities characteristic of the magma and surrounding rock; synthetic diamonds are grown at high temperatures and pressures from a solid solution of (typically) graphite and a metal catalyst in the presence of a diamond seed crystal and may, in principle, include any impurities characteristic to the catalyst, gaskets, anvils, air present during assembly, etc. Natural diamonds are generally classified as boart (ground-up, diamond-like material), industrial (crystals of poor quality or purity), and gemstones. Synthetic diamonds are generally classified as polycrystalline diamond (PCD), single crystal diamond (SCD), or diamond-like material (DLM). Uncut single crystals are termed rough. Diamond single crystals are historically classified into types based on their IR and UV optical spectra. The differences in these spectra reflect the differences in the type and concentration of impurities.[13] The types and impurity content are summarized in Table 2.1.

Table 2.1 Classsifications of Single-Crystal Diamond

Type	Impurity	Color
Ia	~0.1% N_2, in aggregates	pale yellow
Ib	< 500 ppm N_2, substitutional	pale yellow
IIa	"none"	clear
IIb	Trace B, substitutional	blue white

Not included in this older classification scheme is an allowance for growing diamonds with variable ^{13}C content, which can dramatically change the thermal properties. (The natural atomic fraction of ^{13}C is 1.07%.) Type IIa diamonds are those most often considered for use as x-ray mono-chromators.

Because of the wide range of impurities, diamonds are often quoted as having a rather broad range of values of their physical properties (see for example the appendix of ref. 13, which also appears—essentially verbatim—in the Dubbledee Harris Diamond Corp. publication "Properties of Diamonds"). One should bear in mind that these numbers are meant to reflect the range of values one encounters in good- and poor-quality gemstones. High-quality gemstones (particularly synthetic crystals with a uniform and well characterized impurity content) may have well determined and well measured physical properties.

2.2 The Lattice Parameter

As discussed above, natural diamonds show a wide range of impurity content (primarily nitrogen in high x-ray-quality diamonds), and synthetic diamonds can in principle be produced with a range in the value of the ^{13}C to ^{12}C ratio (isotopic purity has been found to improve the thermal properties of diamond by as much as 60%.) As the variations in these quantities and the

temperature affect the lattice parameter, a_o, it is convenient to give here an approximate expression for this dependence:

$$a_o \simeq 3.56715\text{Å} - 5.3 \times 10^{-4} \text{Å } X_{^{13}C} + 3.14\text{Å } X_{N_2} + 3.6 \times 10^{-6} \text{Å } \text{K}^{-1} (T - 298\text{K}), \qquad (2.1)$$

where $X_{^{13}C}$ (is the atomic fraction of ^{13}C and X_{N_2} is the atomic fraction of N$_2$. Here we have simply added the room temperature thermal expansion coefficient[14] and the experimentally measured nitrogen impurity dependence of Kaiser and Bond[15] to the (presumably more accurate) ^{13}C concentration dependent lattice parameter measurements of Holloway et al.[16] For natural ^{13}C abundance, T=298K, and zero nitrogen, a_o =3.56714±0.00005 Å.

The diamond lattice parameter is smaller than that of silicon or germanium. The consequences of this upon the energy cutoff and monochromator tuning range are discussed in Section 3.2.

2.3 Bulk Thermal and Mechanical Properties

The principle thermal and mechanical constants of interest in the design of a monochromator crystal and mount are the thermal conductivity k, thermal expansion coefficient α, lattice constant a_o, and the elastic constants, c_{ij}. We summarize these quantities here for ease of discussion.

Diamond has the best thermal conductivity, from cryogenic temperatures to at least several hundred degrees Kelvin, of any existing material. Because diamond is an electrical insulator (or, at best, type IIb diamond, a semiconductor), the heat is carried principally by the phonons not the electrons. The high thermal conductivity is due to the strength of the diamond covalent bond, which results in a high Debye temperature (2000K) and therefore a reduced number of populated phonon modes near and below room temperature. This reduces the phonon-phonon scattering contribution to the thermal resistance. The thermal conductivity is of course very sensitive to phonon impurity scattering and so the nitrogen, boron, and ^{13}C (or ^{12}C concentration for samples enriched in ^{13}C) can significantly reduce the thermal conductivity. Figure 2.1 shows the average experimental thermal conductivity of type I, type IIa, and type IIb natural isotopic abundance diamond (lines) suggested by ref. 17, as well as some more recent values including one for isotopically pure ^{12}C-diamond from ref. 18. The values of ref. 17 "...are for high-purity, high-perfection, water-white diamond and are thought to be accurate to within 10% of the true values at temperatures above 100K." The various data are tabulated in Appendix A for convenience. Three estimates of the thermal expansion coefficient of diamond,

$$\alpha(T) \simeq \frac{1}{L_{T=0K}} \frac{\partial L(T)}{\partial T}, \qquad (2.2)$$

are given in Fig. 2.2. The recommended values of ref. 17 (circles in Fig. 2.2 and Table A.2) agree well with the more recent suggested fourth-order polynomial fit,

$$\alpha \simeq \alpha_0 + \alpha_1 T + \alpha_2 T^2 + \alpha_3 T^3 + \alpha_4 T^4, \qquad (2.3)$$
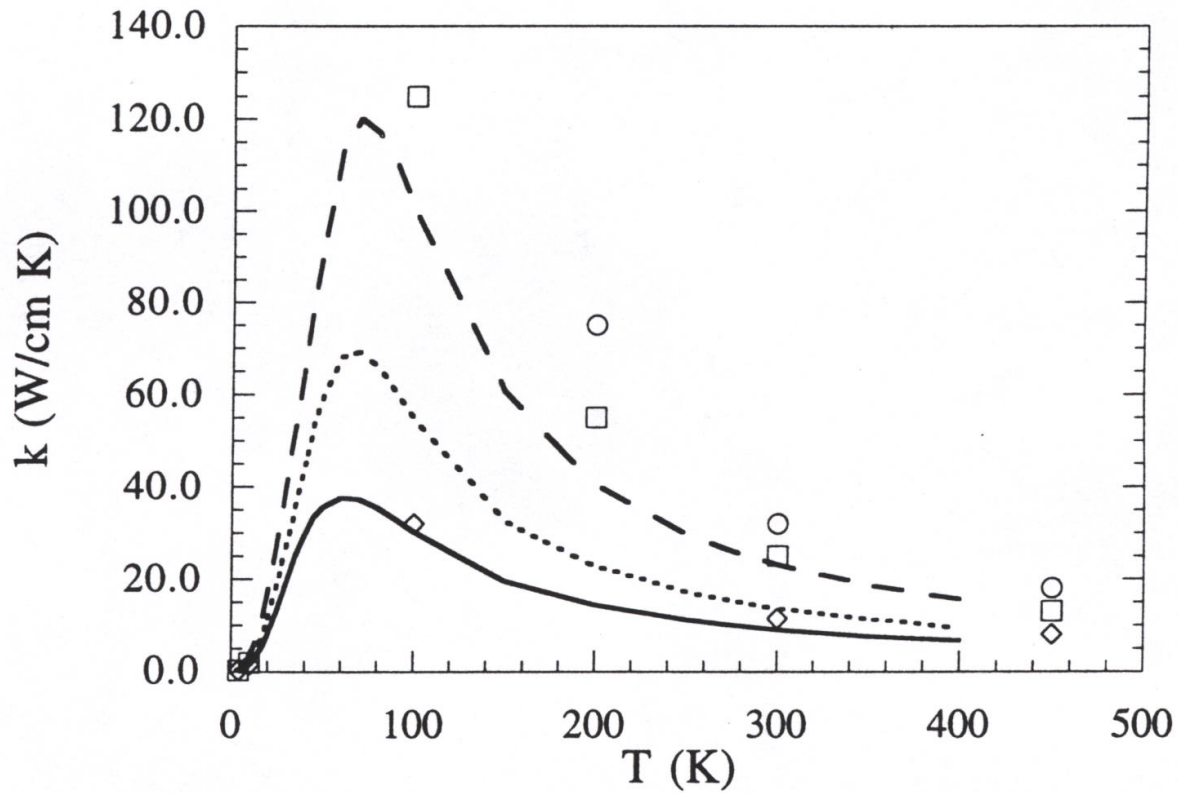
Figure. 2.1. Recommended experimental average of the thermal conductivity (k) of type I (solid), type IIa (dashed), type IIb (dotted), natural isotopic abundance diamond as a function of temperature from ref. 17 from 1970. Also shown are recent (1994) experimental values for type Ia (mean value, diamonds), type IIa (best value, squares), and isotopically pure ^{12}C (circles) diamonds from ref. 18. The values are tabulated in Appendix A.

of ref. 19 (solid line Fig. 2.2) but disagree with the second-order polynomial fit one obtains by differentiating the third-order polynomial expression for $L/L_{293\ K}$ in ref. 17. The coefficients of both fits are given in Table 2.2.

Table 2.2. Coefficients for polynomial expansions of the linear thermal expansion coefficient of diamond [see eq. (2.3)].

Coefficient	Ref. 17	Ref. 19
α_0	-5.912×10^{-7}	0.00
α_1 (K^{-1})	$+6.641 \times 10^{-9}$	$+5.05 \times 10^{-10}$
α_2 (K^{-2})	-1.663×10^{-12}	-5.04×10^{-12}
α_3 (K^{-3})	-	$+7.79 \times 10^{-14}$
α_4 (K^{-4})	-	-1.01×10^{-16}

In order to calculate in detail the deflection of a diamond plate due to mounting strains or direct coolant pressure, it is necessary to know the elastic constants. For rough estimation, only a knowledge of an average Young's modulus is necessary. The experimental elastic moduli and temperature coefficients[20] are given in Table 2.3.

Table 2.3. Elastic moduli and temperature coefficients for diamond.

Modulus	Value (10^{11} N/m^2)	$\dfrac{1}{c}\dfrac{\partial c}{\partial T}$ (10^{-5} K^{-1})
c_{11}	10.79 ± 0.05	-1.37 ± 0.2
c_{12}	1.24 ± 0.05	-5.70 ± 1.5
c_{44}	5.78 ± 0.02	-1.25 ± 0.1

Young's modulus along the (111) direction is

$$E_{11} = \frac{1}{S_{11}} = \frac{(c_{11} - c_{12})(c_{11} + 2c_{12})}{c_{11} + c_{12}} \quad (10.5 \pm 0.1) \times 10^{11}\ Nm^{-2} \quad , \qquad (2.4)$$

and Poisson's ratio is found to vary between 0.1 and 0.29 with an average value of $\bar{\nu}$ 0.2 .[14]

2.4 Typical Surface and Lattice Plane Morphology

Many aspects of the performance of a diamond HHLM are affected by the state of the physical surface of the diamond (to be distinguished from the state of the bulk atomic, or lattice, planes): the thermal boundary resistance depends on the contact surface area; the thermal contact of
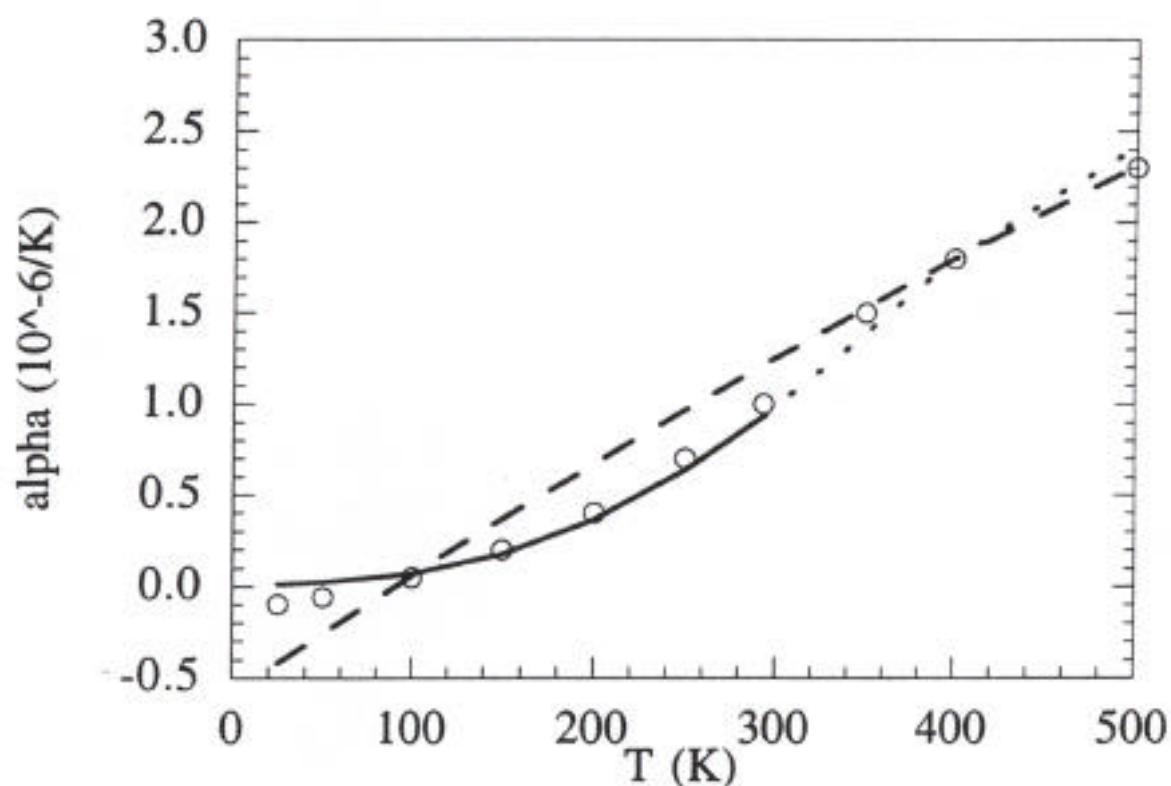
Figure. 2.2. Thermal expansion coefficient, , of diamond as a function of temperature, T. Recommended values of ref. 17 (circles) agree well with the more recent suggested 4th-order polynomial fit of ref. 19 (solid line) but disagree with the 2nd-order polynomial fit (dashed) one obtains by differentiating ref. 17's 3rd-order polynomial expression for L/L_{293K}. The extrapolation of the 4th-order fit of ref. 19 (dotted) is in reasonable agreement with the data to 500K.

clamped plates depends on the surface roughness; and the deflection of a thin diamond crystal plate is often dominated by strain induced when a cylindrically or spherically cut surface is clamped to a flat cooling block.

The state of the bulk atomic lattice planes also has a direct impact on the diffraction performance of a HHLM as lattice distortions can decrease the reflectivity, increase the energy bandpass, and decrease the brilliance of the x-ray beam. It is convenient for the following discussions to decompose the lattice distortions into d-spacing gradients parallel and perpendicular to the lattice plane of interest (as occurs in nonuniform crystal growth), short- and long-range bowing of the lattice plane (characterized by an overall figure or an rms slope error), and mosaic structure (characterized by an rms mosaic angle spread), which we reserve to denote (in the original sense) comparatively perfect sub-crystals separated by rapid changes in the lattice as at a grain boundary or line defect. Synthetic diamonds generally have a true mosaic spread (as defined above) compared to float-zone silicon crystals, which can have essentially no grain boundaries and very low dislocation densities.

As a preliminary survey of such problems, surface and lattice plane measurements were performed on several diamonds currently in possession of the APS staff. The surface roughness measurements were performed with a WYKO TOPO-3D surface profilometer. Measurements were taken at several regions on the front and back surface of the diamond. The profilometer has a 5x objective that samples a 2.05 mm x 2.05 mm area with a pixel size of 8 μ, and a 40x objective that samples a 0.256 mm x 0.256 mm area with a pixel size of 1 μ. Lattice plane bowing was examined by measuring the deviation of the center of the diamond (400) double-crystal rocking curve (Si (531) first crystal) as an x-ray beam was rastered across the surface of the diamond.[21] Figure 2.3 shows a typical diamond surface as seen by the WYKO profilometer with the 5x and 40x objectives. The surface and lattice plane bowing information is summarized in Table 2.4.

2.5 The Liquid-GaIn/Diamond Interface

Achieving a strain- and vibration-free mounting of the first crystal that is also mechanically rigid and provides a good thermal mounting can be a daunting task. Because of the high thermal conductivity of diamond, indirect cooling may be practical. Therefore one solution that has been pursued is to use the surface tension of a thin liquid gallium-indium (GaIn) eutectic to hold the crystal in thermal contact to a cooled copper substrate. (A eutectic of gallium and indium was used to ensure that the liquid metal would remain liquid at room temperatures, which is near the freezing point of pure liquid gallium, and thereby reduce strain in the diamond from differential thermal expansion of the diamond and substrate.) This solution is currently in use on several beamlines at the ESRF. In order to explore the viability of this mounting scheme for the APS, one needs to know several properties of the liquid GaIn—diamond interface at the temperatures that the first crystal is likely to experience. Unfortunately, very little on this subject can be found in the literature.

The first quantity of interest is the thermal *boundary* heat transfer conductance, h_b, which characterizes the thermal conductance at the GaIn/diamond and GaIn/heatsink interfaces. For an assumed uniform, heat flux, the temperature drop across the interface, T, the heat flux q", and h_b are related by the equation
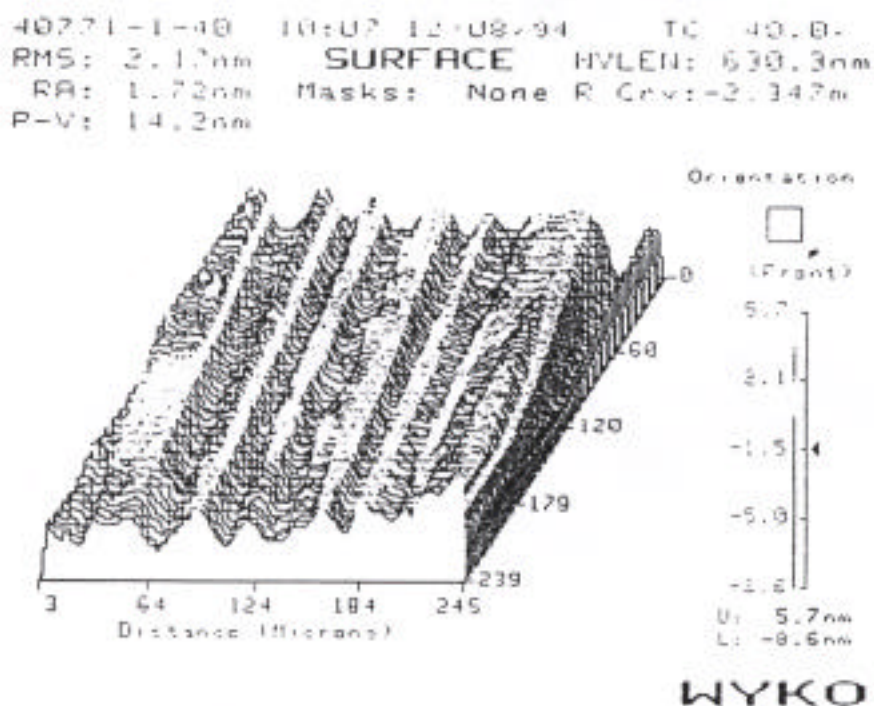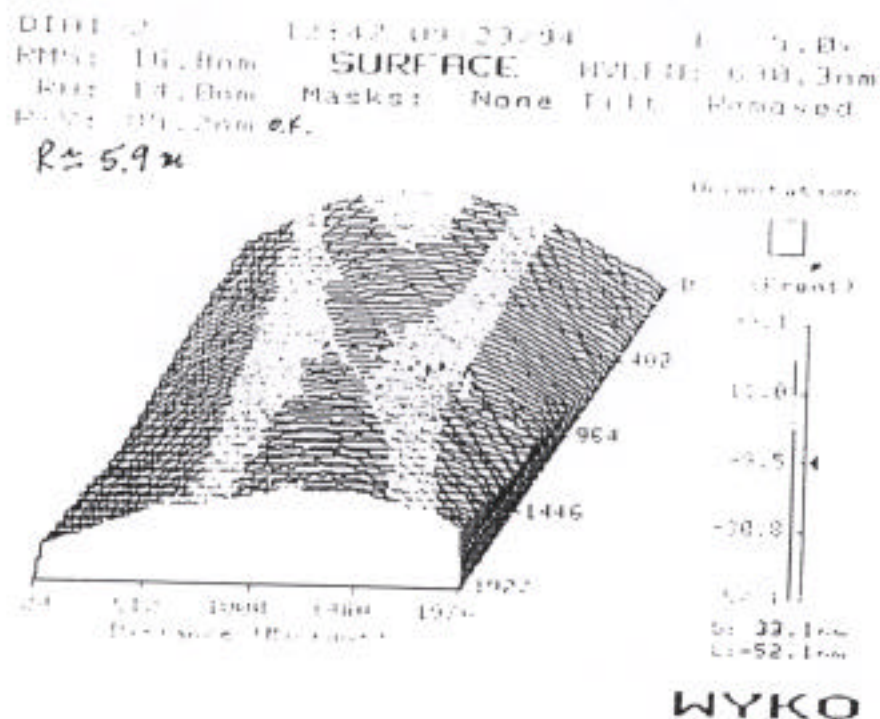
$$q" = P/A = h_b \, T \tag{2.5}$$

Figure 2.3. Surface of two diamonds as measured by a WYKO model TOPO-3D profilometer with (top) 5x and (bottom) 40x objectives. The top crystal is a type IIa (100) oriented seed from Sumitomo (courtesy T. Ishikawa, Spring-8), the bottom a type Ib (111) oriented plate from Sumitomo (courtesy of R. Hewitt EXXON Corp).

Table 2.4. Surface and lattice plane characteristics of several diamonds.

Characteristic	Diamond 1		Diamond 2		Diamond 3	Diamond 4	
Vendor	Sumitomo (Side 1) Courtesy of A. Khounsary, APS	Sumitomo (Side 2)	Harris (Side 1) Courtesy of P. Illinski, APS	Harris (Side 2)	Sumitomo Courtesy of T. Ishikawa, SPring 8	Sumitomo (Side 1) Courtesy of R. Hewitt, Exxon	Sumitomo (Side 2)
Type	Syn. Ib	Syn. Ib	Nat.	Nat.	Syn. IIa	Syn. Ib	Syn. Ib
Approx. Size (mm³)	6 x 6 x 0.3	6 x 6 x .3	5 x 5 x 1	5 x 5 x 1	4 x 4 x 1	7 x 3.5 x 0.5	7 x 3.5 x 0.5
Approx. Shape	square plate	square plate	truncated triangular plate	triangular plate	square plate	rectangular plate	rectangular plate
Orientation	(100)	(100)	(111)	(111)	(100)	(111)	(111)
Cutting Method	laser	laser	cleaved	cleaved	-	-	-
Approx. Surface Figure	Cyl. + Sph.	Cyl. + Sph.	-	-	Cyl.	-	-
Surface Curvature‡ (m)	-2	-5 to -6	-	-	+7	-	-
Surface Roughness (nm, rms at 5x)	20-80	4-40	-	-	8-17	-	-
Surface Roughness (nm, rms at 40x)	2	2	-	-	1-3	-	-
Approx. Lattice Plane Figure	flat	spherical†	-	-	flat	-	-
Lattice Plane Curvature (m)	>200	30	-	-	-	-	-
Mosaic Spread (μrad, rms)	-	-	40-50	40-50	≤4	-	-

† Lattice plane figure due to mounting of crystal.

‡ Positive radii are convex, negative radii are concave.

Here P is the total power transmitted across the interface of cross sectional area A.

To our knowledge, there are no published *experimental* data on the boundary heat transfer conductance between GaIn and diamond (or for that matter GaIn and copper). In a recent publication,[5] a value for h_b of 0.04 W/mm^2-K was assumed. This value, the extrapolated zero velocity intercept of Fig. 3 of ref. 22 is not a heat transfer conductance of a static pure Ga/silicon interface (as suggested) but rather includes the effects of the bulk thermal conduction to the center of the assumed array of 5 mm x 5 mm square cooling channels.

Although taken out of context when applied to a static, GaIn/diamond, planar-geometry interface, indirect experimental evidence indicates that this number may be close to the true value.[23] As has been pointed out by Hart,[24] a value of h_b of 0.04 W/mm^2-K would lead to sizeable temperature gradients (100˚C) under the maximum heat load of APS undulator A. We have thus begun an effort to measure this important quantity.

In order to obtain preliminary measurements in a timely fashion, the prototype split bar measuring device of Fig. 2.4 was constructed. Two 25.4-mm-diameter copper rods were machined down to a 6 mm diameter over a 70 mm length, and the ends were machined to slip fit into a 25.4 mm O.D. stainless-steel alignment tube (1.0-mm-thick wall). The mating ends of the copper rods were machined flat. Three 0.9-mm-diameter holes were drilled 20 mm apart in the conduction rods to accommodate the stainless-steel clad thermocouple probes. A 250 W heater strap was wound around the top of the device during operation. A variable transformer was used to adjust the electrical power. It is desirable to place such devices in vacuum, but, in order to obtain preliminary results quickly, the device was wrapped with an insulating glass-fiber blanket. This blanket and the stainless alignment tube reduce convective and radiative heat losses.

The heat transfer coefficient is measured (see left side of Fig. 2.4) by producing a linear heat flow through the gap between the rods. The heat flux is calculated from the measured temperature drop across the known distance between each thermocouple in the top and bottom rods. By assuming a linear (or other model) heat drop in the rods, one can estimate the temperature drop across the gap. Subtracting temperature drops due to previously measured interfaces and bulk conductances, one can obtain an estimate of the temperature drop across the interface of interest. Dividing the heat flux by this number yields the boundary heat transfer conductance, h_b.

Initially pure liquid gallium was coated on the ends of the copper conduction rods. In order to get the gallium to wet the copper, it was necessary to sand and heat the surface. The device was assembled with liquid gallium filling the 0.080 mm gap between the rods, and the heat transfer coefficient was measured (see Table 2.5). Next, diamonds were put in the device and measured. Again it was important to clean and heat the surface while scrubbing the gallium in with the wooden end of a cotton swab. To ensure that the thermocouples gave the same reading at a given temperature, they were all immersed in ice water and then boiling water after the experiment was completed. The results of the measurements are given in Table 2.5. In all cases, the inferred temperature drops are only a couple of degrees or less and may be significantly affected by the assumed temperature independence of the copper thermal conductivity, as well as other systematic errors. The quoted numbers should therefore be taken as preliminary, order-of-magnitude estimates. Preparations are now underway to perform a more precise measurement under a vacuum environment.
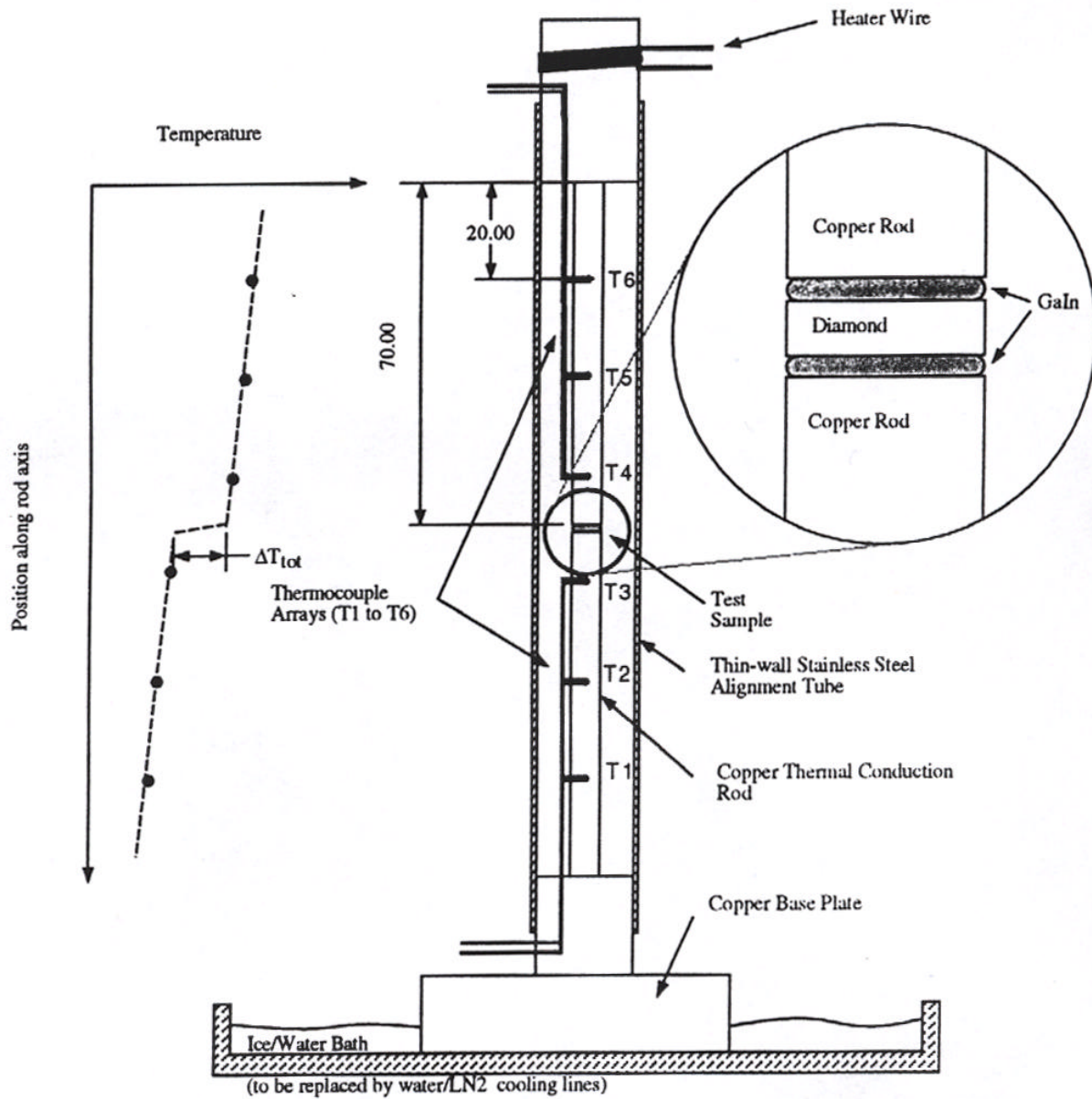
Figure. 2.4. Split bar device used to measure the liquid GaIn/diamond boundary heat transfer conductance, h_b. A large temperature gradient (150 - 200°C) is placed across the two bars and the temperature drop across the gap is inferred from the temperature drop along each bar. The (assumed linear) heat flux across the gap divided by the inferred temperature drop across the interface yields an estimate of the heat transfer coefficient, h_b.

Table 2.5. Results of boundary heat transfer conductance measurements. T_6 and T_1 are temperature readings by the thermocouples T_6 and T_1 (see Fig. 2.4), Q" is the heat flux at the interface, ΔT_{tot} is the temperature drop across the entire joint, T_{joint} is the approximate temperature at the center of the joint (taken equal to $(T_6+T_1)/2$), ΔT_b and h_b are, respectively, the temperature drop and the heat conductance at the interfaces Cu-Cu or diamond-Cu with a Ga layer as a heat transfer medium (here ΔT_b is equal to ΔT_{tot} minus the contributions of diamond, when present).

Expt. N°.	Total Heat Path	Q" (W/mm^2)	$T_6 - T_1$ (°C)	T_{joint} (°C)	ΔT_{tot} (°C)	Measured Interface	ΔT_b (°C)	h_b (W/mm^2.°C)
1	Cu-Ga-Cu (OFHC copper)	0.49	186.4 - 61.1	124	1.4	Cu-Ga-Cu	1.4	0.35*
2	Cu-Ga-Diam-Ga-Cu (Diamond IIb, 0.3-mm thick)	0.5	187.1 - 58.9	123	3.3	Diam-Ga-Cu	1.6	0.31
3	Cu-Ga-Diam-Ga-Cu (Diamond IIa, 0.5 mm-thick)	0.95	198.2 - 88	143	4.5	Diam-Ga-Cu	1.9	0.50

* Note that there is a gap, 0.08 mm wide, between the tips of the OFHC Cu rods (see text), and this gap is filled with liquid gallium. Therefore this number includes the contribution of conduction through the gallium thickness.

If liquid metals for thermal contact are to be used, the corrosion rates of diamond and copper in liquid Ga or GaIn eutectic could be important parameters. Again, little quantitative information is available, and so we have begun a series of measurements. The results of the initial measurements indicate that diamond is not quickly dissolved by liquid Ga even at 250˚C. Optical measurements of a diamond surface after 2 and 6 hour exposures to pure liquid Ga at 250 ± 20˚C seemed to indicate pitting of the diamond surface at a rate of approximately 50 nm/hr in localized spots, but cleaning of the surface followed by a third optical measurement found the pits to have disappeared.[25] At present, the situation has not been sorted out and simply requires systematic study.

3.   DIFFRACTION PROPERTIES OF DIAMOND

In order to better understand the possibilities and limits of proposed diamond HHLM designs, it is useful to recall and examine some of the basic absorption and diffraction properties of diamonds compared to silicon for typical APS undulator beams.

3.1 Reflection Widths and Integrated Reflectivities

3.1.1 The Bragg Geometry

The angular range over which the reflection curve is near unity is called the Darwin width and, for zero absorption, is given by:

$$\omega_D = 2\, r_e\, F(hkl)\, \lambda^2 / \pi V \sin (2\theta), \tag{3.1}$$

where r_e is the classical electron radius, $F(hkl)$ the structure factor for the hkl reflection, λ the wavelength, V the volume of the unit cell, and θ the Bragg angle. Figure 3.1 shows the Darwin width of several low-order symmetric reflections of diamond, silicon, and germanium along with the vertical opening angle of APS insertion devices and bend magnet sources for comparison. Figure 3.2 shows the corresponding Darwin energy width

$$E_D = \omega_D\, E \cot (\theta) \tag{3.2}$$

as a function of energy.

The width of the reflectivity curve can also be expressed in terms of temperature variation, i.e., $T_D = \omega_D/(\alpha \tan \theta)$, where α is the coefficient of thermal expansion. This is an indication of the temperature difference that can be tolerated across the face of the crystal transverse to the beam direction and still diffract from the second (similar) crystal of a double-crystal monochromator. When the expression for the Darwin width is substituted in the expression above, it can be seen that this width, when expressed in terms of temperature, is independent of x-ray energy for a given reflection:

$$T_D = [-1/\alpha][4r_eF(hkl)d^2 / \pi V] \tag{3.3a}$$

$$= [-1/\alpha][4r_eF(hkl) / \pi a_0(h^2 + k^2 + l^2)] . \tag{3.3b}$$

Table 3.1 shows the energy and temperature Darwin widths for the low order Si, Ge, and diamond reflections. The linear thermal expansion coefficients used were $1.0 \times 10^{-6}\ °C^{-1}$ (@ 293K) for diamond and $2.6 \times 10^{-6}\ °C^{-1}$ (@293K) for silicon.[17]
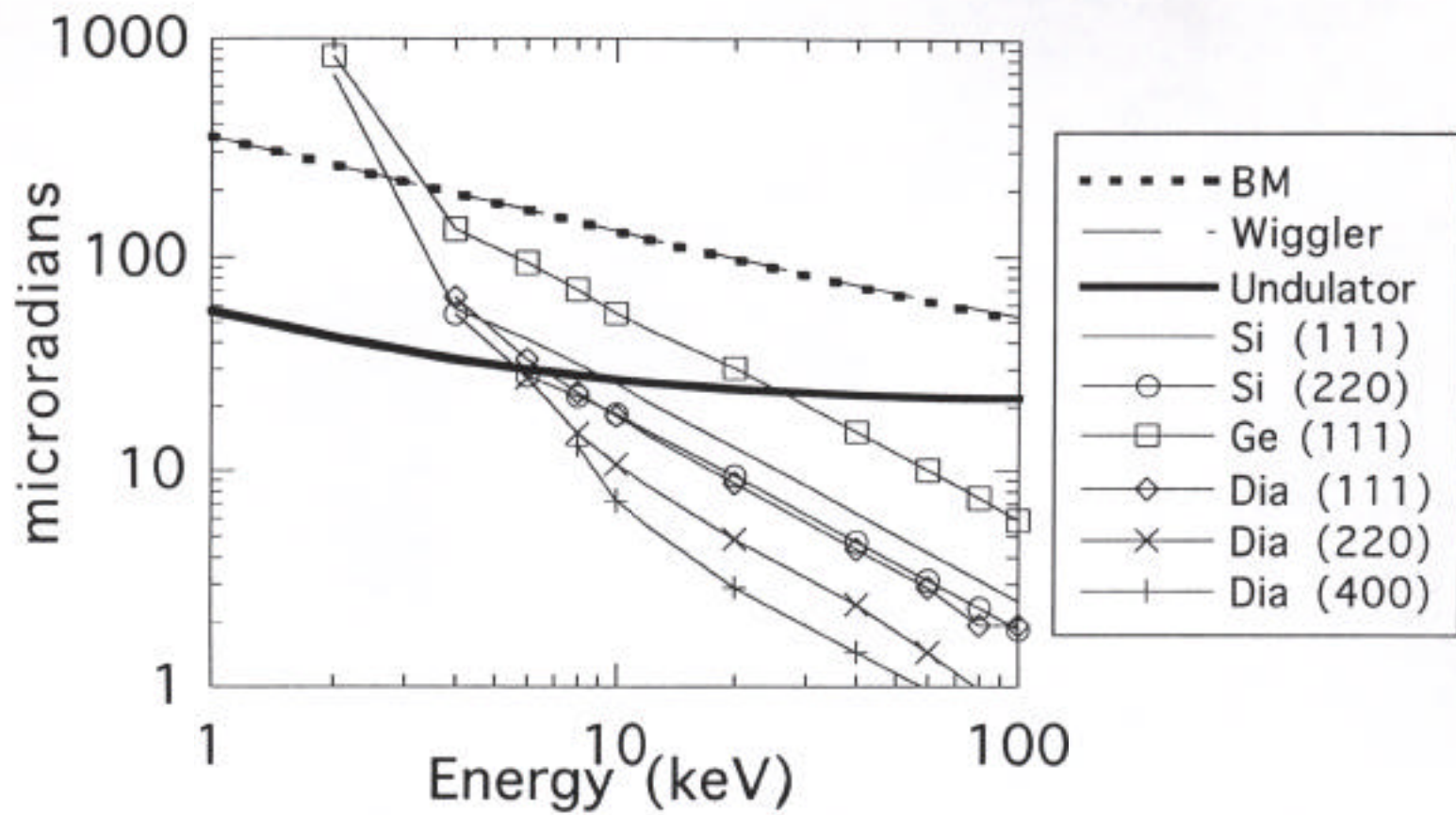
Figure 3.1 The Darwin widths of several diamond, silicon, and germanium reflections are plotted as a function of energy. Also plotted is the FWHM opening angles of the bending magnet, wiggler and undulator beams.
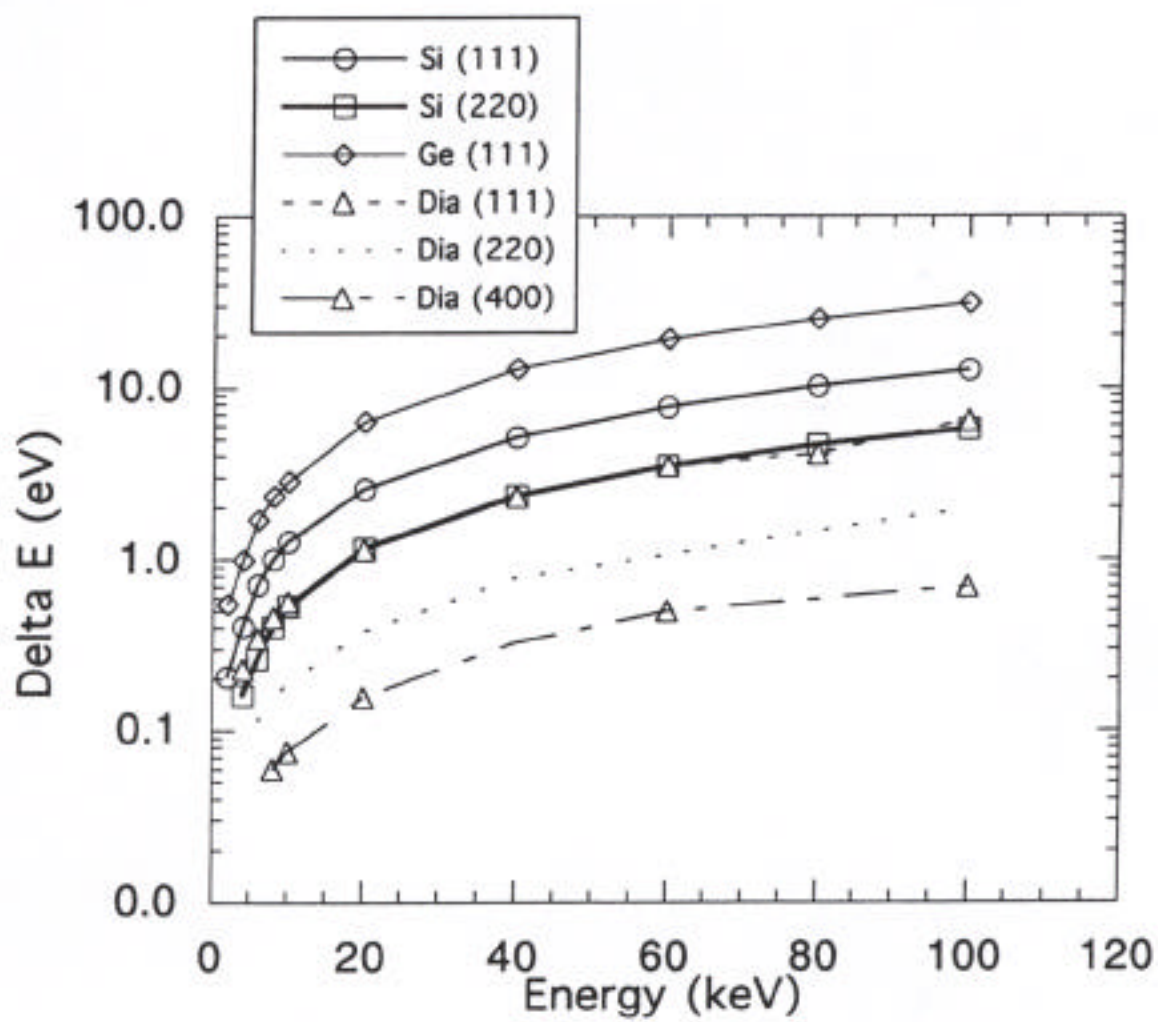
Figure 3.2. Energy widths of several diamond, germanium, and silicon reflections as a function of energy.

Table 3.1. Bragg geometry reflection widths and integrated reflectivities of several diamond and silicon reflections at 10 keV.

Reflection	T_D	E_D/E	R(E)dE	R^2(E)dE	Ratio
	(°C)	(x10^{-6})	(eV)	(eV)	
Diam (111)	59	62	0.809	0.635	0.51
Diam (220)	20	19	0.24	0.199	0.16
Diam (400)	8	7	0.093	0.077	0.063
Si (111)	59	133	1.629	1.236	1.00
Si (220)	25	56	0.685	0.531	0.43
Si (400)	11	25	0.278	0.212	0.17

Ignoring mosaic spread and strain, the throughput of a single-crystal monochromator should (to a very good approximation) be proportional to the integral of the dynamical diffraction reflectivity curve R(E), which includes the non-negligible effects of absorption:

$$1 \text{ Crystal Throughput} \qquad R(E) \, dE. \qquad (3.4)$$

Likewise the throughput of a double-crystal monochromator (with the same first and second crystals) should be proportional to the integral of the square of the reflectivity curve:

$$2 \text{ Crystal Throughput} \qquad R^2(E) \, dE. \qquad (3.5)$$

Table 3.1 shows the Bragg geometry integrated reflectivity and integrated square reflectivity at 10 keV. The last column gives the ratio of the integrals of the square reflectivity of each entry relative to that for Si (111). Note that the energy integrated reflectivity of the diamond (111) reflection is a factor of 2 less than the Si (111) reflection and produces a significant loss of usable flux on sample as compared with silicon. The losses for the higher Q diamond reflections are, for most, unacceptable, and therefore the remainder of this document focuses primarily on monochromators using the diamond (111) reflection even though, as mentioned earlier, [100] oriented diamond plates are the most readily available.

The integral of the reflectivity curve and of the square of the reflectivity curve for the diamond (111) and silicon (111) reflection are shown in Figure 3.3. The ratio of the integral of the diamond (111) reflectivity curve to the integral of the silicon (111) reflectivity curve and the ratio of the integral of the square of the diamond (111) reflectivity curve to the integral of the square of the silicon (111) reflectivity curve are shown in Figure 3.4. The structure factor information used in the above calculations is summarized in Appendix B.

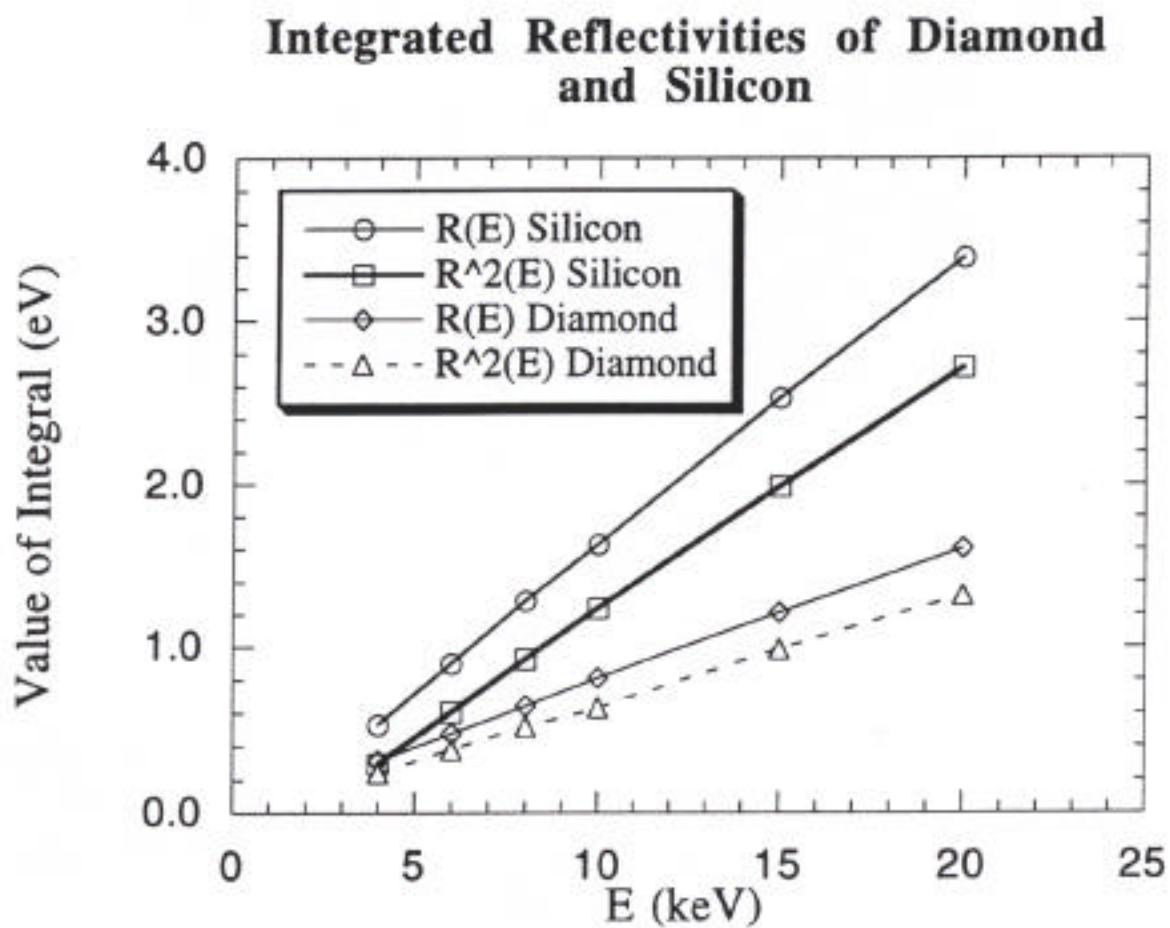## Integrated Reflectivities of Diamond and Silicon

Figure 3.3. Integrated, Bragg geometry, one crystal $[R(E)]$ and two-crystal $[R^2(E)]$ energy reflectivity curves for diamond (111) and silicon (111).

Ratio of Diamond Integrated Reflectivity
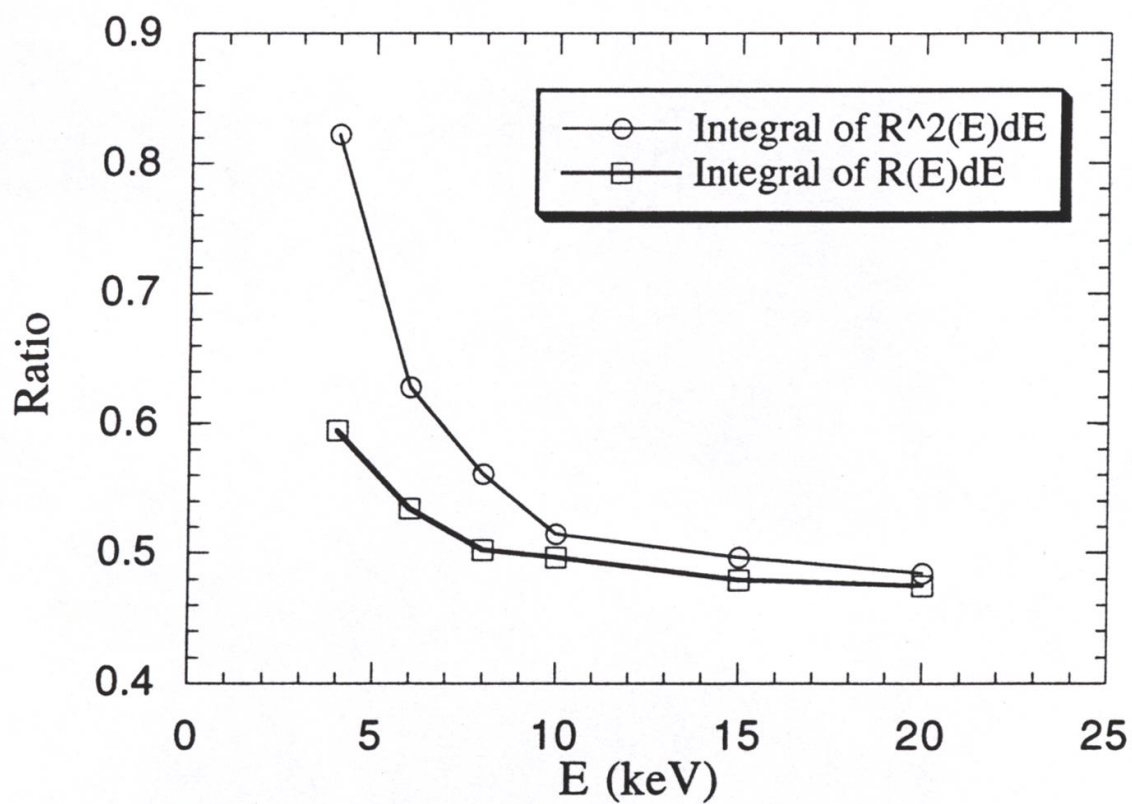## Relative to that of Silicon

Figure 3.4 Ratios of single- and double-crystal diamond (111) reflectivity to silicon (111) reflectivity.

3.1.2 The Laue Geometry

Diamond plates whose large face is parallel to the (400) planes can be used in a Laue or transmission geometry to diffract from the (111) planes. The geometry of this arrangement is shown in Figure 3.5 with the angle between the (100) planes and (111) planes equal to 54.74°. This means that the reflection from the (111) planes will be asymmetric and that Eq. (3.1) for the Darwin width must be modified with the inclusion of the asymmetry parameter, b, given by:[26,27]

$$b = \mathbf{n} \cdot \mathbf{s_O} / \mathbf{n} \cdot \mathbf{s_H}, \tag{3.6}$$

where $\mathbf{n}$ is the unit normal of the incident surface, and $\mathbf{s_O}$ and $\mathbf{s_H}$ are unit vectors in the incident and scattered beam directions. The Darwin width for an asymmetric reflections is given by:

$$\omega_D^{asy} = \omega_D / b. \tag{3.7a}$$

A corollary to this is that the size of the beam also changes when asymmetric crystals are used.

$$y^{asy} = \{ b \} \, y \, . \tag{3.7b}$$

where Y is the size of the incident beam. Depending on the arrangement of the crystal with respect to the incident beam, the asymmetry can be used to increase the input acceptance or to narrow the physical size of the outgoing beam (if only a single Laue reflection is used) as has been done at the Troika beamline at the ESRF. The primary disadvantage of the Laue geometry is that, except for very thin crystals, the diffracted beam power is shared equally between the two exit beams, the so-called diffracted and forward-diffracted beams. This loss could be made up through increased acceptance when the asymmetry parameter, b, could be made smaller than 0.25. As can be seen from Figure 3.6, only over a very small energy range can b be made less than 0.25.

Figure 3.6 shows the asymmetry parameter versus energy for the diamond (111) reflection and the various asymmetry angles that naturally occur with a (100) or (110) oriented diamond in Laue and Bragg geometry. At small grazing-incidence or exit angles, the crystal surface has to be extremely flat to retain good reflectivity. Because of this fact (and matching of first and second crystals if a two-crystal device is to be used), the monochromator design becomes very problematic for b values with

$$|b| < \frac{1}{10}, \text{ or } 10 < |b|. \tag{3.8}$$

Figure 3.7 summarizes the effects of the various geometries on the beam size, divergence, and transmission.
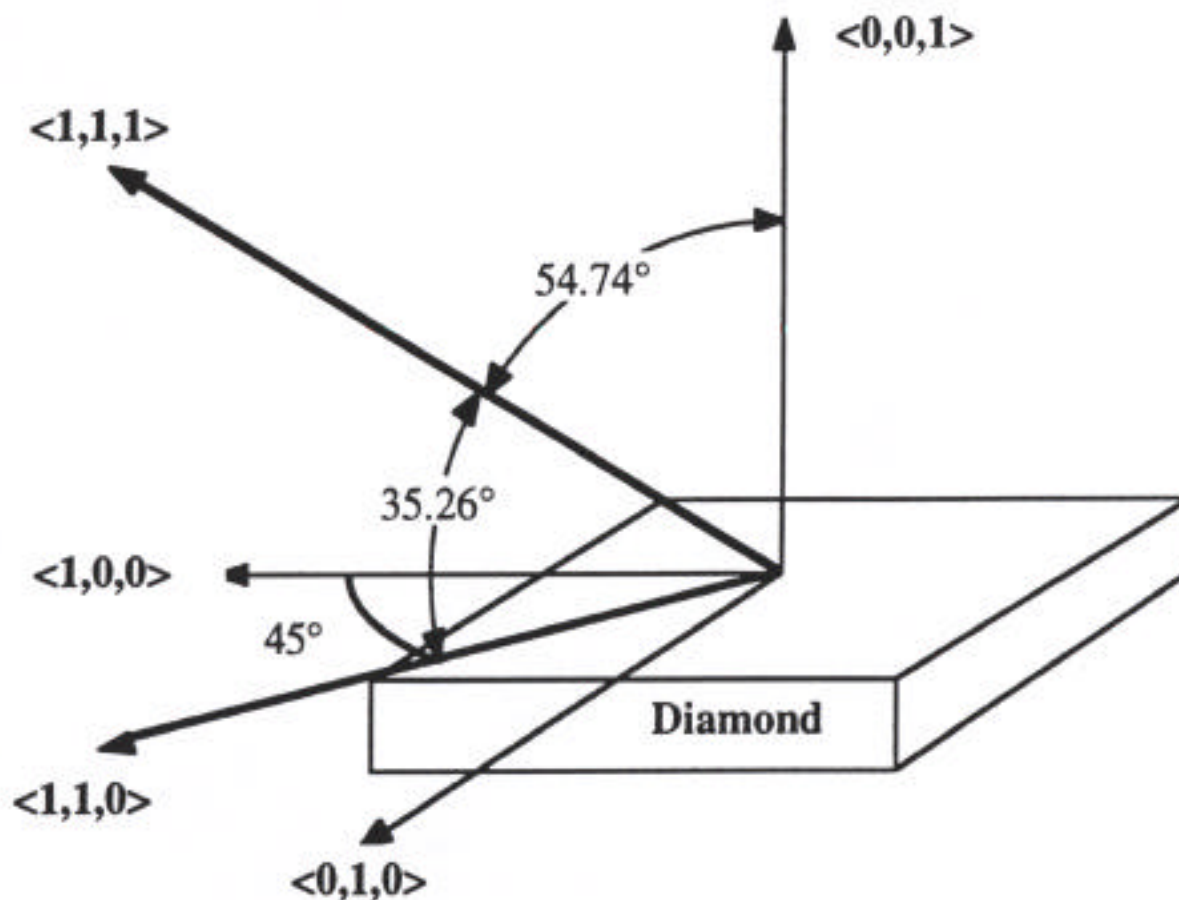
Figure 3.5. Orientation of <111> and <110> conventional cubic cell reciprocal lattice vectors in a <001> oriented diamond plate such as is commonly obtained from synthetic diamonds. The inclination angle of the (111) planes to the (001) surface is 54.74˚.
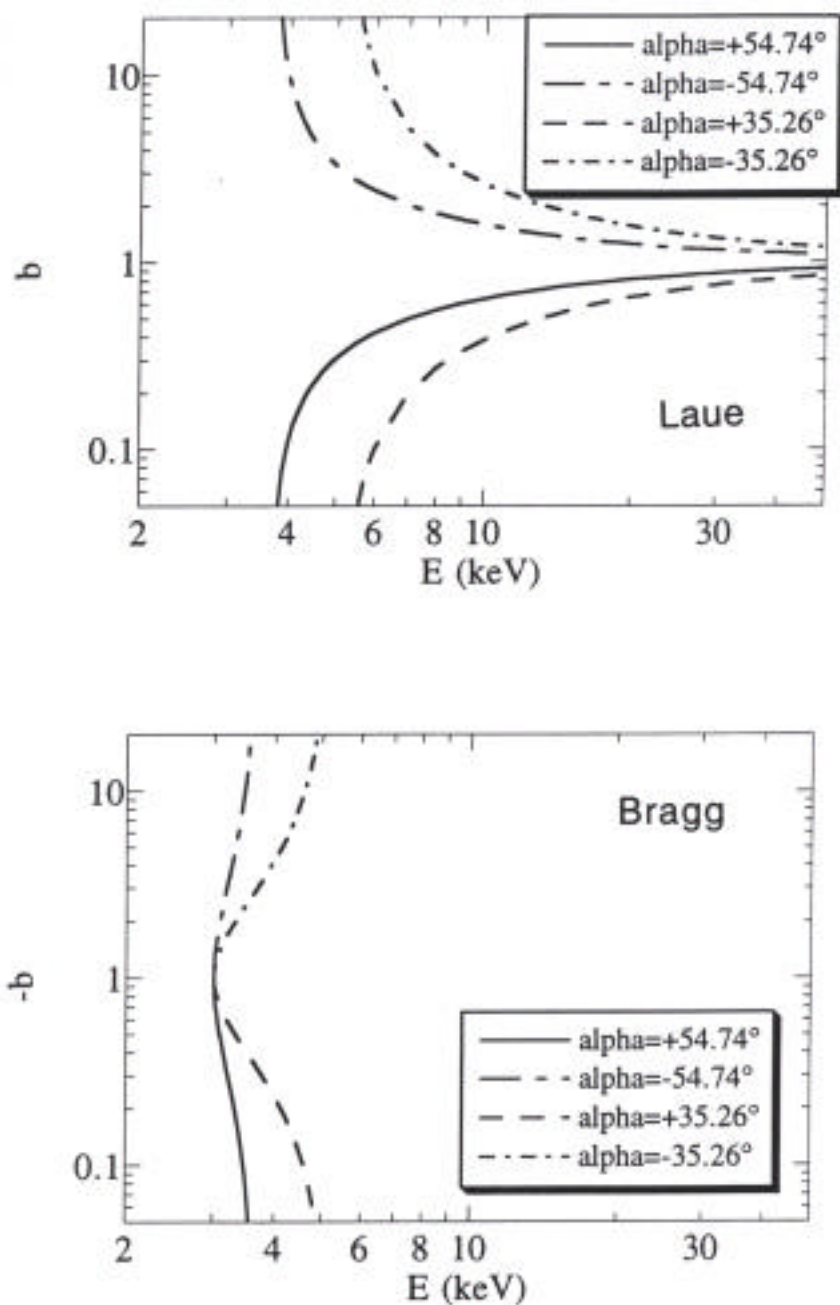
Figure 3.6. Asymmetry parameter b for diamond (111) Laue (top plot) and Bragg (bottom plot) geometry reflections for conventional asymmetry angles naturally present in (100) and (110) oriented diamond plates.

Bragg Geometry
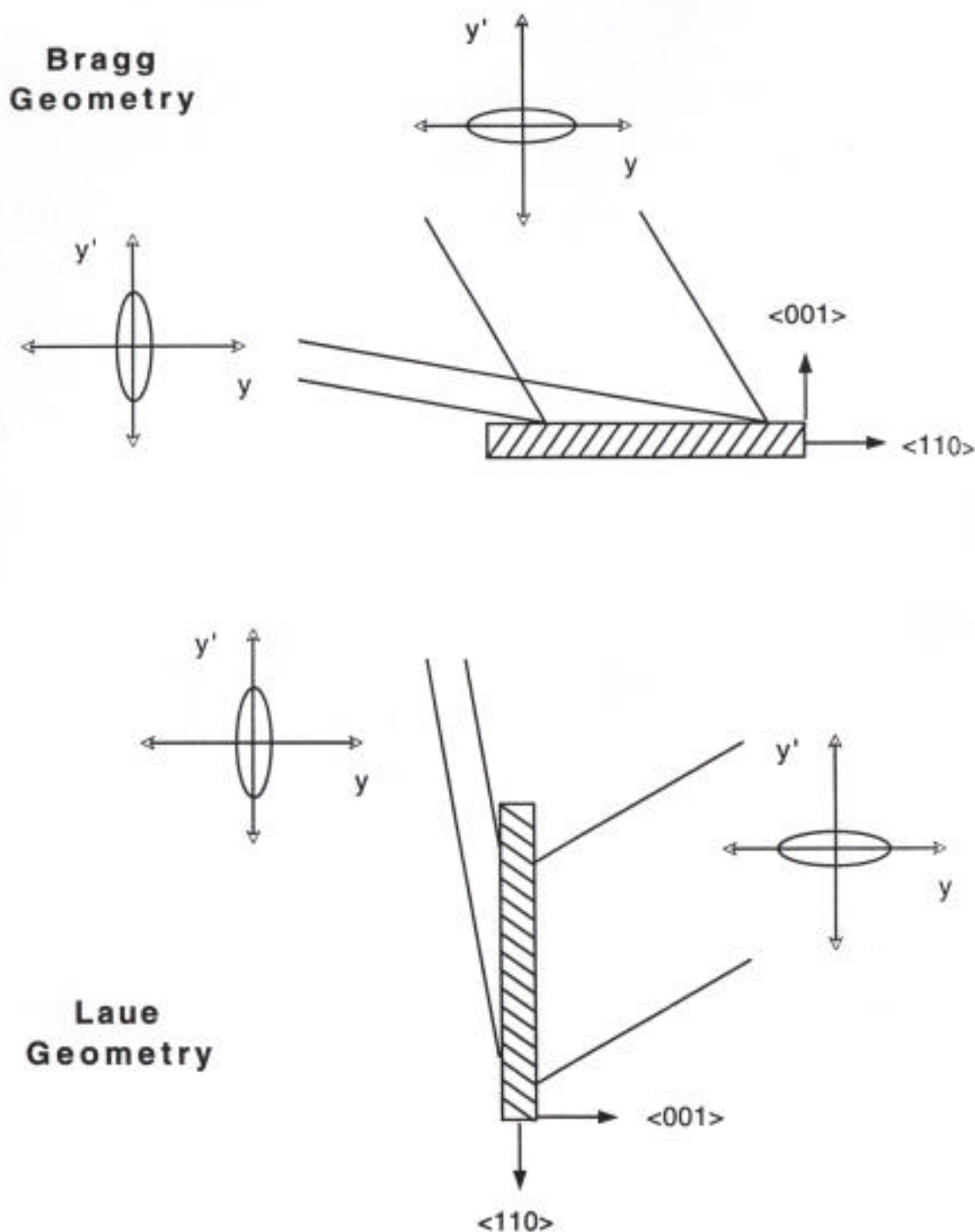
Laue Geometry

Figure 3.7. Schematic of the beam geometries for an asymmetric reflection from the (111) planes in a plate whose faces are parallel with the (001) planes in both the Bragg and Laue geometries. Also shown are schematics representations of the phase space of the incident/diffracted x-ray beams. Here y' denotes the angular acceptance and y the spatial extent of the beam.

3.2 Reflection Geometry, Cutoff Energies, and Tuning Range

Although silicon and germanium both have the diamond lattice structure, diamond has a smaller conventional cubic unit cell constant, a_o, and therefore a *higher* low-energy cutoff, E_c, in the Bragg reflectivity:

$$E_c = \frac{hc}{2a_o} \sqrt{H^2 + K^2 + L^2}.$$ (3.9)

Here h is Plank's constant, c is the speed of light, and **H**, **K**, and **L** are the Miller indices. This increase in the cutoff energy limits the range of operation of a diamond monochromator. Table 3.3 lists the cutoffs of diamond, germanium, and silicon for three of the lowest order reflections. The mechanical operations of the monochromator will typically limit the Bragg angle to less than or on the order of 60°, and so the practical cutoff energy will be increased about 15% above the theoretical limits of Table 3.3.[14,28,29]

Table 3.3. Lattice parameter, a_o, and Bragg energy cut-offs, E_c, of Diamond, Ge, and Si.

Crystal	a_o	E_c (keV) for the Given Reflection		
	(Å at 25°C)	(111)	(220)	(400)
Diamond	3.56714 [14]	3.010	4.916	6.952
Germanium	5.65782 [28]	1.898	3.099	4.383
Silicon	5.43106 [29]	1.977	3.229	4.566

One consequence of the smaller lattice constant of diamond is that the motion of the second crystal in a fixed-exit-beam-height design, double crystal monochromator is reduced (see Fig. 3.8). For the choice of the location of the common Bragg angle rotation axis shown in Fig. 3.8, the total translation along Z2 required between 4 and 20 keV for a vertical offset of 35 mm is 93 mm for diamond (111) compared with 142 mm for silicon (111). This could, in principle, allow a significant reduction in the size and weight of the typically rather bulky second-crystal mechanism.

3.3 Absorption

One of the most attractive features of diamond is its low x-ray absorption cross section, which can be used to allow a significant fraction (if not the majority) of the x-ray beam power to be transmitted through a diamond monochromator first crystal and deposited in an isolated beam stop. This is to be compared to the case of silicon and germanium, where essentially all of the incident x-ray beam power is deposited as heat in the first crystal. This decreased heat load in the first crystal further reduces distortions of a first diamond crystal compared to a first silicon crystal.

Figures 3.9 and 3.10 show this dependence for the total absorbed power and peak absorbed power density of an unfiltered Undulator-A beam incident on symmetric (111) Laue and Bragg geometry crystals for a variety of thicknesses, t. The undulator is assumed to be tuned so that
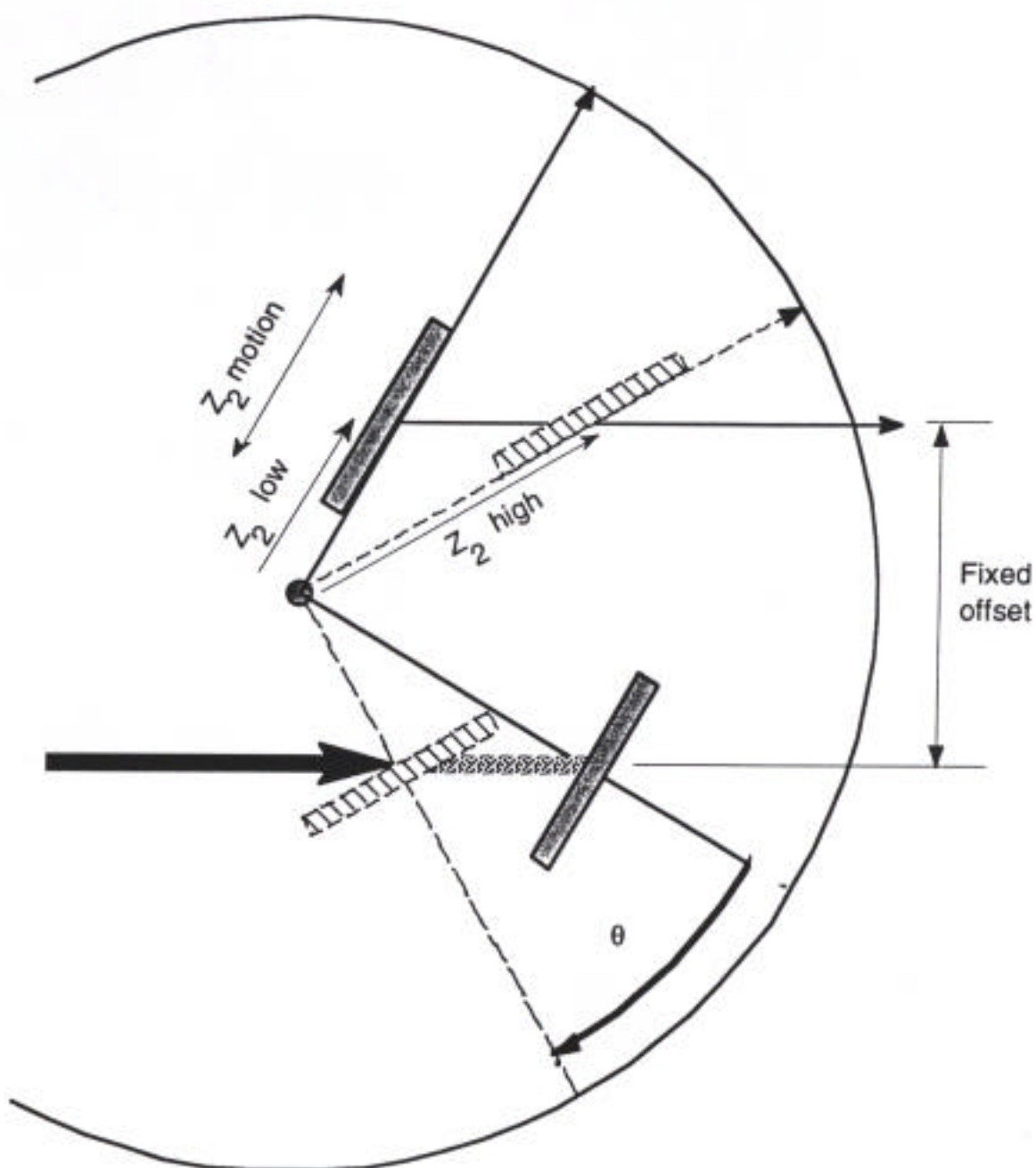
Figure. 3.8. Second crystal motion of a fixed-exit double-crystal monochromator with a common Bragg angle rotation axis at the intersection of the normal to the first crystal surface and a line extended along the surface of the second crystal. The required travel of the second crystal along the Z_2 axis as the energy is changed from E_{low} to E_{high} is $Z_{2\ high} - Z_{2\ low}$.

a)
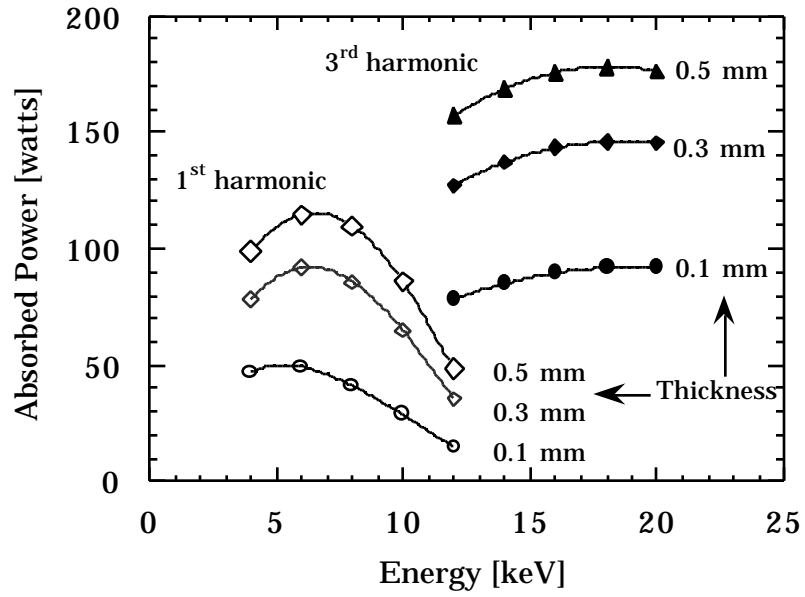
b)
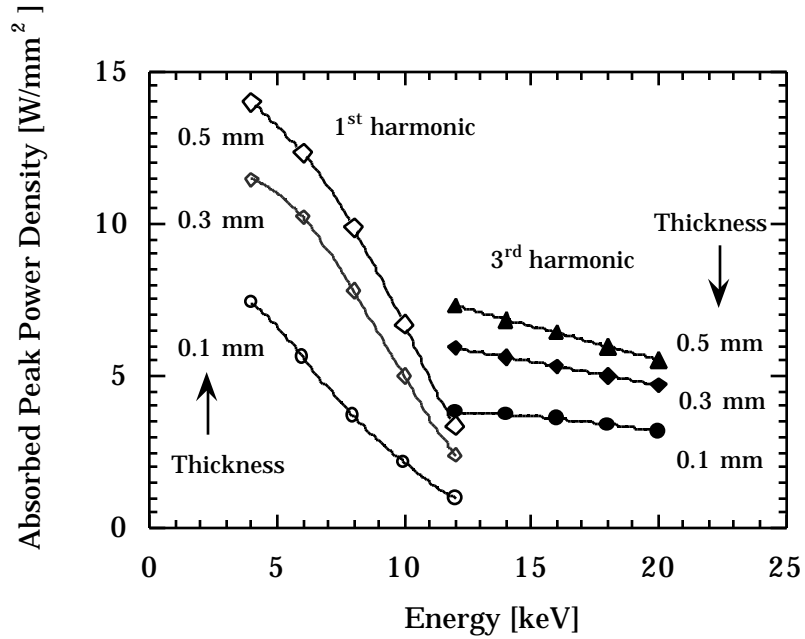
Figure 3.9. (a) Absorbed total power and (b) absorbed peak power density for symmetric Bragg geometry (111) diamonds of various thicknesses. The specified undulator harmonic as well as the monochromator bandpass are assumed tuned to the specified energy. No filters were assumed for the third-harmonic tunings, and so these estimates are conservative.

a)
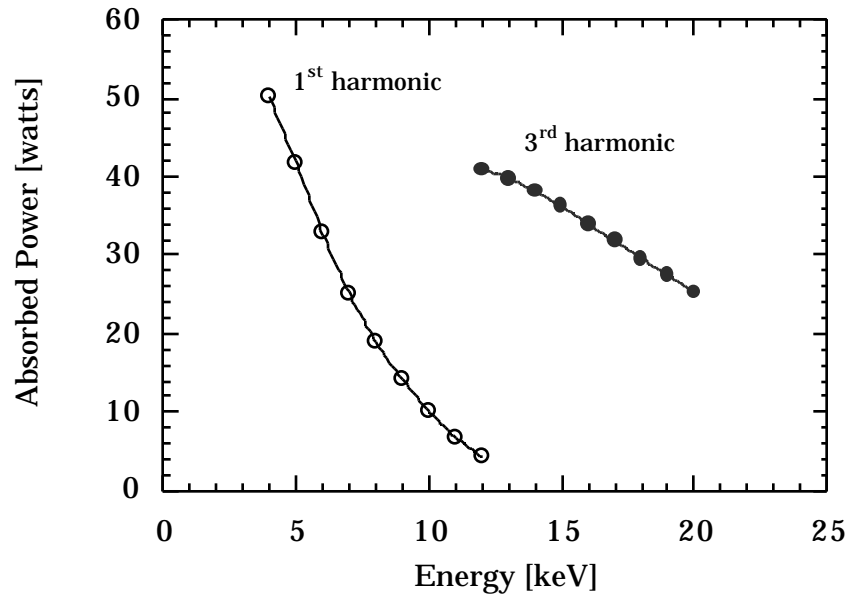
b)
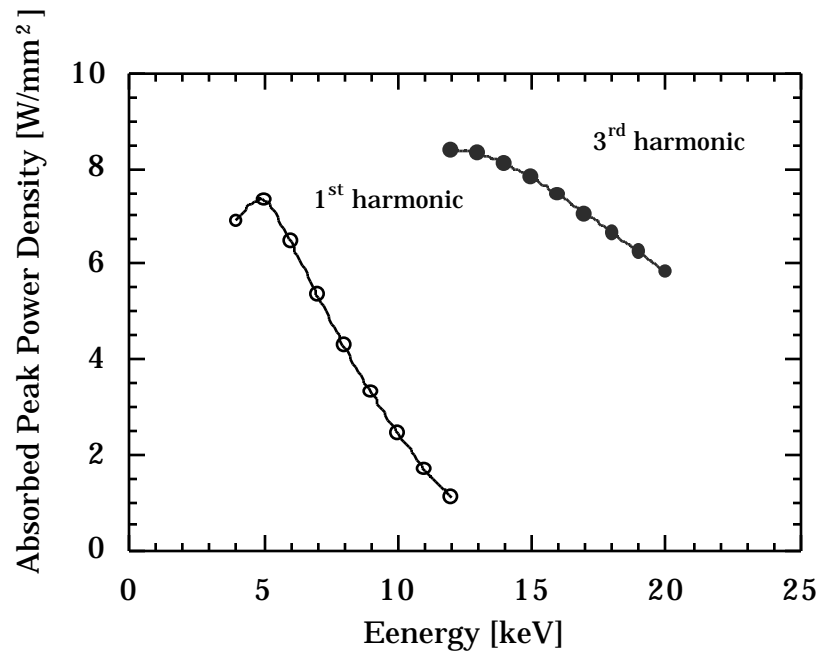
Figure 3.10. (a) Absorbed total power and (b) absorbed peak power density for a symmetric Laue geometry (111) diamond of 0.1 mm thickness. The specified undulator harmonic, as well as the monochromator bandpass, are assumed tuned to the specified energy. No filters were assumed for the third-harmonic tunings, and so these estimates are conservative.

the peak of the first (or third) harmonic coincides with the monochromator energy. The calculations are made for a storage ring energy and current of 7 GeV and 100 mA, respectively. The monochromator crystal is 30 m from the source, and a mask immediately upstream of the first crystal is assumed to define the beam to 1.5 mm vertical x 3.6 mm horizontal. The calculations were made using the UA program.[30] The results of the calculations are also tabulated in Appendix C for convenience.

3.4 Non-Diamond Second Crystals

Because of the small size of good diffracting diamonds, double-crystal monochromators (DCM) employing a diamond second crystal will require a more precise, motorized translation stage than is needed for a Si DCM in which the beam can be allowed to walk across the surface of the second crystal. The small size of a diamond second crystal also makes the design of a bending mechanism for sagittal focusing more problematic. These reasons have led some designers to contemplate the use of a non-diamond second crystal.

Because the source divergence in the plane of diffraction (normally the vertical plane) is very narrow, the losses due to dispersion mismatch can be kept to an inconsequential level if a relatively close d-spacing match between the diamond and the second crystal can be obtained. Table 3.4 shows the d-spacing mismatch for the first three allowed reflections in diamond and several closely matched silicon and germanium reflections. Here $\Delta d/d = (d_X - d_C)/d_C$, where d_C is the diamond d-spacing and d_X is the Ge or Si d-spacing.

Table 3.4 d-spacings of diamond, Si, and Ge reflections at 25 ˚C.

Reflection	d (Å)	$\Delta d/d$
Diam (1,1,1)	2.059	-
Si (2,2,0)	1.920	-0.068
Ge (2,2,0)	1.996	-0.029
Diam (2,2,0)	1.261	-
Si (3,3,1)	1.246	-0.003
Ge (3,3,1)	1.295	+0.029
Diam (4,0,0)	.8918	-
Si (5,3,1)	.9180	+0.029
Si (6,2,0)	.9543	+0.072
Ge (5,3,1)	.8587	-0.037
Ge (6,2,0)	.8927	+0.003

Perhaps the largest impact of a slightly dispersive geometry is that the twice diffracted beam will no longer be parallel to the incoming beam. Figures 3.11a - c show the angular deviations $2\Delta\theta = 2\theta_{B2} - 2\theta_{B1}$ from parallelism that the twice diffracted beam will experience relative to a non-dispersive arrangement. For moderate angular deviations, the twice reflected beam could be redirected parallel to the incident beam through the use of a post monochromator mirror.

The use of non-identical first and second crystals would also provide enhanced harmonic rejection over the normal configuration of two identical crystals because the angular separation of the first and third harmonics are different if the d-spacings are not the same. Figure 3.12 shows the reflectivity curves for the first and third harmonics from diamond (111) and (333) (the second harmonic is diffracted from the forbidden (222) reflection and is not plotted) and two possible second crystal candidates, Si (220) and Ge (220). In this figure, the first harmonics have been aligned to provide maximum throughput. Note that the overlap of the reflectivity profiles of the third harmonics are sufficiently misaligned to have minimal throughput. This property may be particularly important when using high critical energy beamlines, such as those encountered at the APS.

3.5 Beam Multiplexing

The use of Laue (transmission) geometry monochromators using thin (0.1 mm) diamond crystals is being pioneered by Als-Nielsen and others on the TROIKA beamline at ESRF.[31] The goal is to multiplex the x-ray beam so that several hutches on the same beamline can operate simultaneously as is done commonly with neutron beams at thermal neutron research reactors such as the Institute Laue Langevin (ILL) in Grenoble.[32] (The various symmetric and asymmetric Laue and Bragg geometries were discussed earlier in Section 3.2. It is worth noting that some of these geometries may be advantageous for beam multiplexing as they naturally reduce the path length of the transmitted beam and therefore decrease the beam attenuation.) Such a monochromator would obviously be quite useful on a wiggler line if one could obtain substantially larger diamonds. The advantage, however, is not as clear for undulator radiation, which is concentrated in moderately narrow bandwidth peaks, as several stations operating simultaneously would have a much larger probability of interference. Yet, if one is interested in doing experiments at several *fixed* incident energies lying within the width of an undulator harmonic, there may be significant advantages to this approach. Its true utility will only be known when experience is gained on such lines that actually have multiple monochromators supplying beam simultaneously to multiple experiments.

a)

Diamond (111)

d(c 111) = 2.0595
d(Si 220) = 1.9202
d(Ge 220) = 2.0003

diamond_(111)_deviations.plt

b)

Diamond (220)

d(c 220) = 1.2611
d(Si 331) = 1.2460
d(Ge 331) = 1.2980

diamond_220_deviations.plt
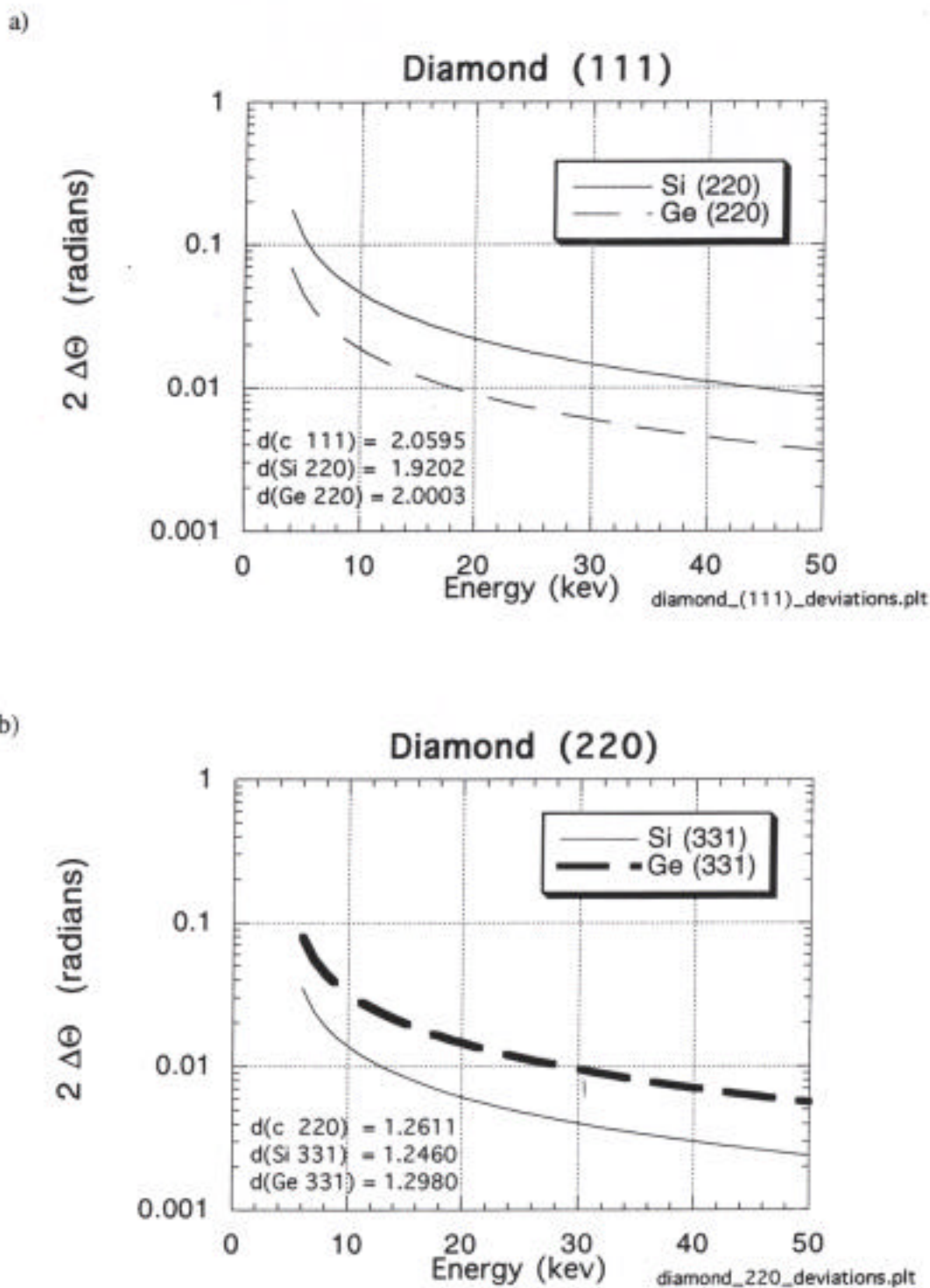
Figure 3.11. Exit beam angular deviation $2\Delta\theta = 2\theta_{B2} - 2\theta_{B1}$ for (a) diamond (111), (b) diamond (220), and (c), and diamond (400) (see page 34) first crystal reflections and the specified second crystal reflection. Bold lines indicate that $2\Delta\theta$ is negative.

c)

Diamond (400)
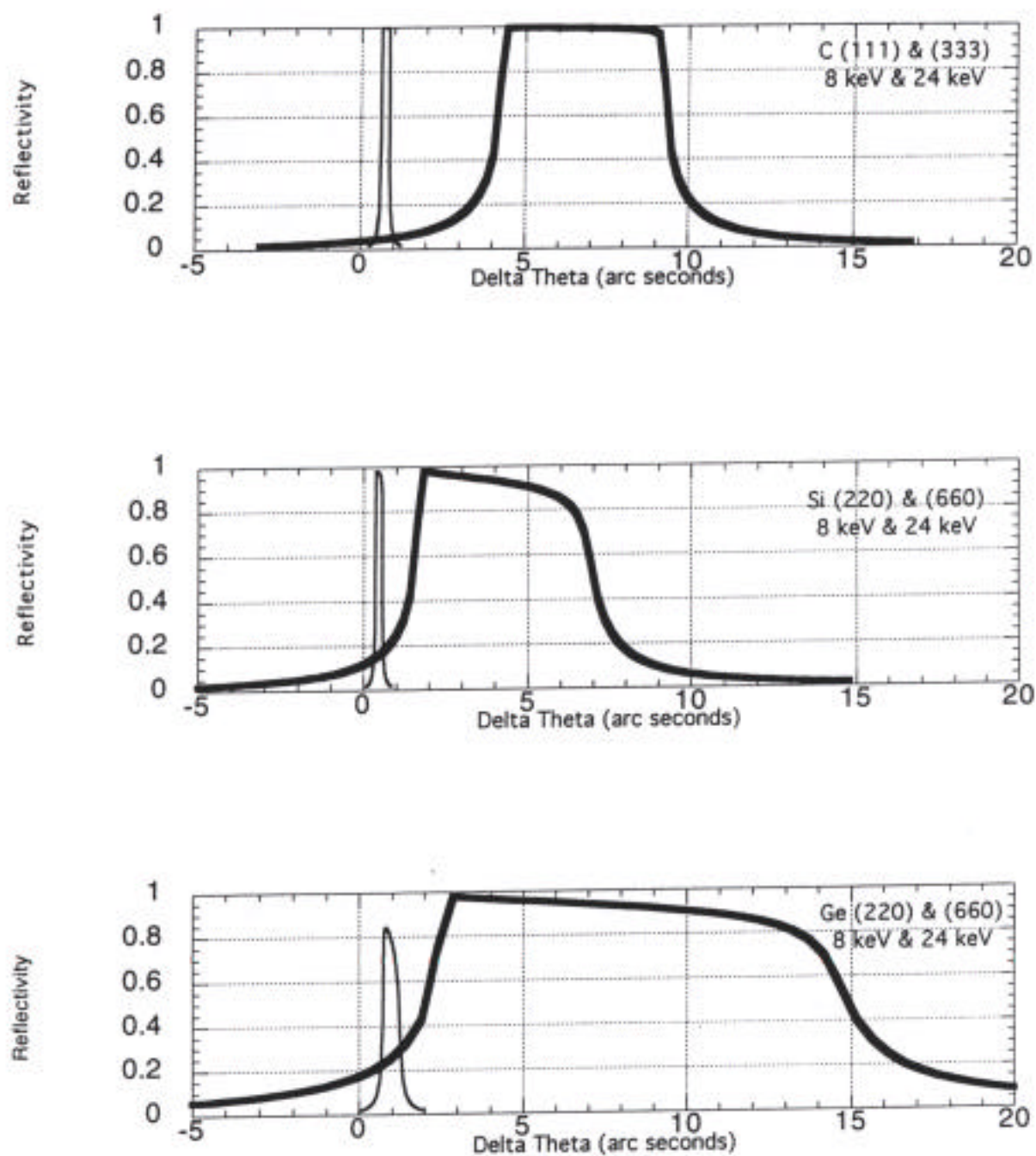
diamond_400_deviations.plt
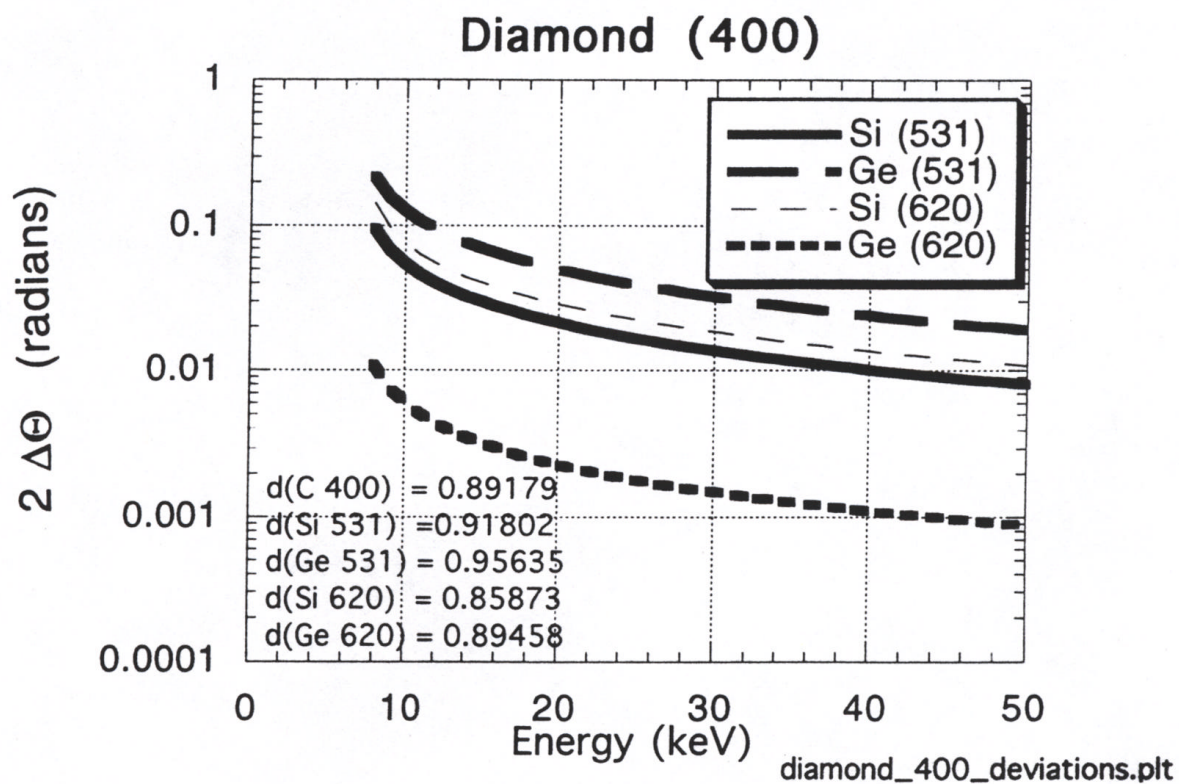
Figure 3.12. Natural harmonic rejection obtained through the use of a non-diamond second crystal. See the text for details.

4.   THERMAL DESIGN OF DIAMOND MONOCHROMATORS

4.1 General Design Constraints

To be useful, the diamond in a diamond monochromator must be mounted in a rigid but strain-free manner and, in the case of a first crystal, be either directly cooled and therefore sealed to a block with cooling channels or indirectly cooled and therefore thermally clamped to a directly cooled block. The temperature of the diamond needs to be stable to within the Darwin temperature defined in Eqn. (3.3) as the storage ring current (and therefore heat load) decays and to be not so large to produce bowing of the crystal. The temperature gradients should also be small enough that they do not produce significant strains/slope error variations within the beam footprint.

As mentioned above, one of the primary advantages of diamond over silicon is that due to its lower absorption length, much of the incident power will be transmitted through the diamond (recall Figs. 3.9 and 3.10). To the extent that this is true, the x-ray beam power will be deposited nearly uniformly within the depth in the diamond, and so the heat flow will be approximately two-dimensional, at least away from the thermal connection to the heat sink.

Ignoring emittance effects and errors in the magnetic field of the undulator, the angular half width of a harmonic peak is

$$\sigma_r \quad \frac{1}{\gamma} \sqrt{\frac{1 + K^2/2}{2Nn}} \quad , \tag{4.1}$$

while the angular half width of the power distribution is 1/ . Here K is the deflection parameter, N is the number of periods in the magnet structure, and n is the harmonic number. The power distribution at the monochromator is thus significantly wider than the distribution of the harmonic peak energy photons. One usually masks off the beam to the rough size of the harmonic peak distribution in order to reduce the total power. Such masks are typically rectangular in shape and, unless designed otherwise, produce a sharp edge to the power profile on the surface of the first monochromator crystal, which causes a corresponding slope error.

Assuming either a square or circular power distribution of uniform intensity, one obtains one of the four following heat flow models. The first is a one-dimensional heat flow in a plate and is appropriate for thin side-cooled diamonds. The second is radial heat flow in a circular plate, which is appropriate when the beam size is small compared to the radius of the heat sink. The last two models are radial heat flow from a half cylinder and radial heat flow from a half sphere appropriate to cases in which the thickness of the diamond is significant compared to the absorption length.

To evaluate the performance of a diamond monochromator under the heat load from the APS Undulator beam, a three-dimensional model of a diamond crystal was developed using the ANSYS[33] finite element analysis code in which a side-cooling scheme was applied. The result of the analyses are presented in Section 4.5. To estimate the temperature gradient on the surface of a diamond monochromator cooled from the sides, one could possibly use a model of a fraction of a centrally heated circular plate cooled at its rim and uniformly heated through the thickness[4] (see Figure. 4.1). The heat conduction equation can be written as follows:

$$Aq'' = 2\pi r t k(T)\frac{dT}{dr} \quad , \tag{4.2}$$

where q" is the heat flux, A the area of the heated spot, k(T) is the thermal conductivity, and t is the thickness. For Type-IIa diamond, the thermal conductivity between 20°C and 127°C can be approximated within 3% error by[17]

$$k(\Delta T) = k_o(1 - \beta \Delta T) \quad , \tag{4.3}$$

with β =0.007807 K^{-1}, where k_o is the thermal conductivity at 20°C (=2.3562 W/mm-K),[17] ΔT is the increase of the crystal temperature (from 20°C, the reference temperature). The solution of Eqn. (4.2) is

$$\Delta T = \frac{1}{\beta}\left(1 - \sqrt{1 - 2\beta \Delta T_o}\right), \tag{4.4}$$

where

$$\Delta T_o = \frac{P}{f_c 2\pi t k_o} \ln \frac{R_2}{R_1} \tag{4.5}$$

is the solution of Eqn. (4.2) for a constant thermal conductivity, $P = \pi R_1^2 q''$ is the total power deposited in the crystal, t is the crystal thickness, R_1 is the radius of the beam footprint, and R_2 and f_c are, respectively, the radius and the fraction of the cooled circumference.

It follows that the temperature difference across the crystal surface depends on the logarithm of the ratio of the crystal size to the beam size. However, this model assumes a circular beam footprint, which is not always the case. The shape of the beam footprint is often rectangular or square with almost uniform heat flux. Therefore, the approximation is accurate only when the beam footprint is much smaller than the size of the crystal. Let us consider the case simulated in Section 4.5 of this document, with the following parameters:

- Size of the beam footprint   3.6 mm x 2.9 mm
- Equivalent beam radius (R_1)   1.82 mm
- Crystal surface area   6 mm x 6 mm
- Cooled area   27.6 mm^2
- Crystal thickness   0.3 mm
- Total absorbed power from Undulator A   92 watts

Using Eqn. 4.5 with an average radius of the cooled area, R_2 , equal to 2.5 mm, and f_0=0.55, we obtain a maximum temperature drop across the crystal of about 12.5°C. The finite element analyses (Section 4.5) give a temperature drop of 15.6°C in the sagittal direction and 9.0°C in the tangential direction.
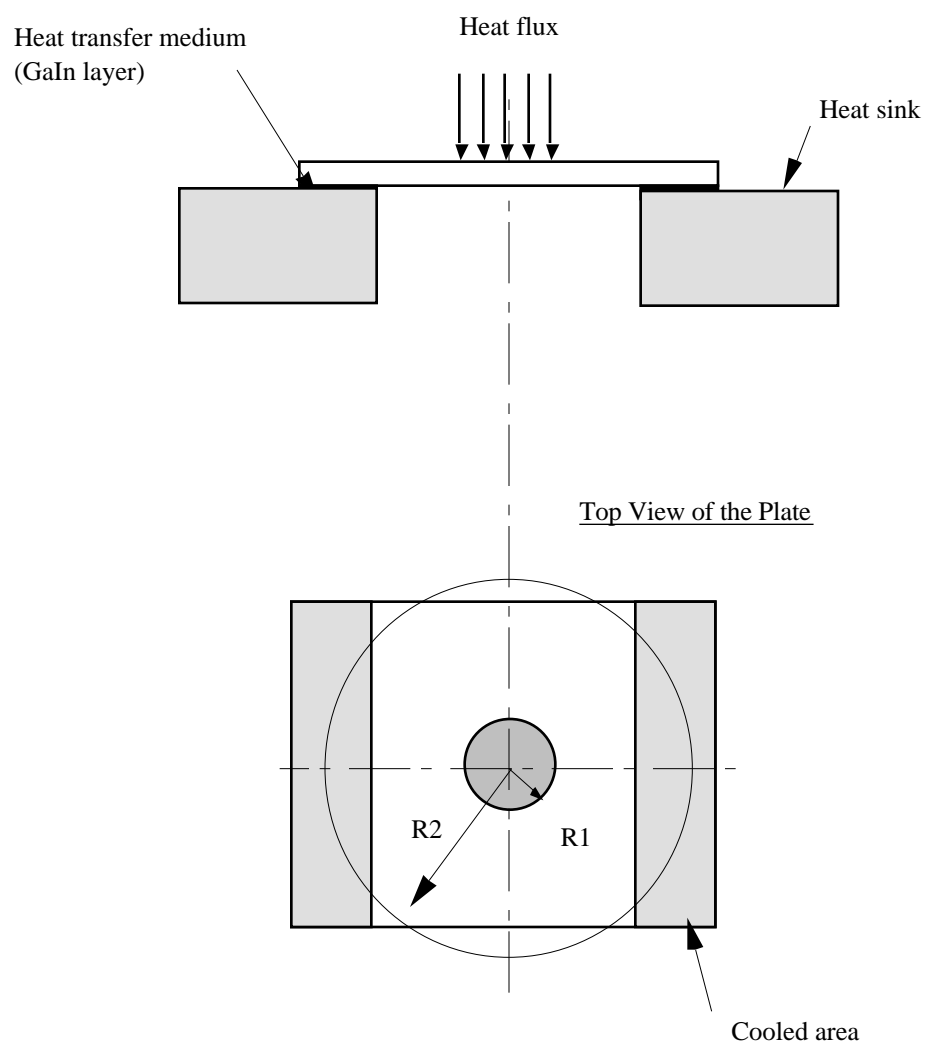
Figure 4.1. Model of a fraction of a centrally heated circular plate cooled at its rim and uniformly heated through the thickness.

4.2 Direct Cooling of Diamonds

Diamonds can be laser machined to high accuracy (±0.001" or better) and in principal could be directly cooled with internal water microchannels or more complex heat exchanger patterns machined into the back of the diamond or water jet cooling on the back face of the diamond as done by Berman and Hart.[6] Whatever the mechanism, diamond provides better heat transport than the cooling material and any practical coolant placed behind the diamond will absorb a significant amount of x-rays thereby worsening the heat loading problem.

4.3 Operation at Cryogenic Temperatures

As is the case with silicon, improved thermal and mechanical performance can be expected with diamond when cooled to cryogenic temperatures. Diamond is an attractive candidate for liquid nitrogen cooling because only a small portion of the total incident power is typically deposited in the diamond, thereby reducing the cooling capacity requirements and liquid nitrogen usage of the cooling system.

Recently several members of the APS staff collaborated with staff members from the ESRF and SPRing-8 on the first tests of a cryogenically cooled, single crystal diamond monochromator. This experiment, coordinated by Hitoshi Yamaoka of SPRing-8, was performed at the BL3 (focused wiggler) line at the ESRF. Mounting strains from the differential thermal expansion severely hampered these experiments with the thin synthetic Type IIa diamond manufactured by Sumitomo Ltd. (diamond size 5 mm x 4 mm x 0.2mm). Nonetheless, narrow rocking curves (3.2 arc seconds), but not at the theoretical values were finally achieved at a diffracted energy of 23.8 keV under incident surface power densities of 90W/mm^2.[34] Although in principle, cryogenically cooled diamonds will out perform diamonds at room temperature, clearly a considerable amount of effort still needs to be invested into this area, particularly in the development of strain-free mountings.

4.4 Cooling through a Liquid Ga/In Layer

One of the simplest ways of mounting diamond crystals strain free, an approach used frequently at the ESRF, is with a thin liquid layer of Ga/In at the sides of the crystal (side cooling).[4] The surface tension of the liquid holds the crystal in place while providing a strain-free, thermal contact to the cooled substrate, often a water-cooled copper block. As mentioned previously, experiments carried out at the ESRF[23] indicate that h=0.04 W/mm^2-K seems close to the value which is consistant with experiments. If that is the case, for a 6 mm x 6 mm x 0.3 mm crystal cooled from two sides with a 1 mm contact-width on the top and bottom faces (i.e., total wetted area equal to about 27.6 mm^2), the temperature drop at the GaIn layer would be more than 160°C for a crystal absorbing 92 watts (the heat transfer coefficient was divided by 2 for the two interfaces: diamond-GaIn and GaIn-copper). The maximum temperature at the center of crystal will increase by roughly the same amount. Because the thermal conductivity and the coefficient of thermal expansion depend on the temperature, the temperature drop across the crystal and the resulting distortions will also increase dramatically. However, if we assume that single-crystal synthetic diamonds of larger sizes up to 1 cm x 1 cm could be available soon, one could increase the wetted area to the point where the temperature drop is acceptable. For example, for an 10 mm x 10 mm diamond crystal with a 0.3 mm thickness (and keeping the same clearance for the incident beam), the contact area may be increased to about 122 mm^2, which reduces the temperature drop to about

36.5°C. The peak temperature will increase to about 84.5°C (= 36.5 + 48), which is still an acceptable value. Moreover, by reducing the crystal thickness, the absorbed power decreases, thereby decreasing the heat flux at the interface. With a 10 mm x 10 mm x 0.1 mm crystal, the temperature difference across the interface will go down to about 21.64°C. In this case, the thermal conductivity and the thermal expansion of diamond will be only slightly affected. Therefore, we expect the temperature gradient and, consequently, the distortions in the crystal to increase only by a small amount.

Table 4.1 summarizes the expected temperature drop across the diamond heat sink interface for various power loads and diamond sizes, when a liquid gallium layer is used as a heat transfer media. The calculation are for Undulator-A beam at K=1.644 and for a diamond (111) crystal set to diffract 6 keV photons (symmetric Bragg reflection) 30 m from the source, with no filters or windows. The beam slits are set to 3.6 mm horizontal by 1.5 mm vertical. The crystal is cooled from two sides and edges. (The front and the back side are free.) The wetted area was calculated assuming the width of the reflecting surface constant and equal to 4 mm (i.e., slightly larger than the horizontal slit opening), the heat conductance at the boundary layer was set at 0.02 W/mm^2-K, and the thickness of the liquid gallium layer was equal to 100 μm, which is much higher than needed.

Table 4.1. The expected temperature drop across the diamond heat sink interface for various power loads and diamond sizes, when a liquid gallium layer is used as a heat transfer medium. The crystal is exposed to the UA beam at 7 GeV-100 mA operation and is oriented to diffract 6 keV photons (symmetric (111) Bragg reflection) with a slit opening of 3.6 mm x 1.5 mm at 30 m from source, and it is cooled from two sides (the front and the back side are free). The wetted area was calculated assuming the width of the reflecting surface constant and equal to 4 mm (i.e., slightly larger than the horizontal slit opening), and the heat conductance was set to 0.02 W/mm^2-K. T_{int} is the temperature drop due the boundary layer; T_{Ga} is the temperature drop due conduction through 0.100 mm thickness of gallium.

Crystal surface	Crystal thickness (mm)	Absorbed power (watts)	Wetted area (mm^2)	ΔT_{int} (°C)	ΔT_{Ga} (°C)	ΔT_{total} (°C)
6 mm x 6 mm	0.1	49.0	25.2	97.9	5.0	102.9
	0.3	92.0	27.6	166.1	10.1	176.2
8 mm x 8 mm	0.1	49.0	65.6	37.4	2.3	39.7
	0.3	92.0	68.8	66.9	4.05	70.95
10 mm x 10 mm	0.1	49.0	122.0	20.1	1.2	21.3
	0.3	92.0	126.0	36.5	2.2	38.7

This table shows the importance of the size of the wetted area/crystal. The temperature drop across the joint diamond heat sink is too high for small crystal sizes and high powers, which might make the crystal useless. Remember, however, that our preliminary measurements, presented in Section 2, indicate that the boundary heat conductance might actually be much larger than the number used in the above calculations. Note that, liquid gallium has a relatively poor thermal conductivity (0.03 W/mm-K at 30°C, to be compared with that of copper, for example, which is about 0.38 W/mm-K). Therefore, it is important to keep the thickness of the liquid gallium (or GaIn eutectic) layer as thin as possible.

One possible way to eliminate the GaIn layer is by directly growing a single crystal or to bond a diamond platelet on a polycrystalline diamond heat sink. Polycrystalline diamond with a thermal conductivity that is 90% that of single crystal can be produced. However, a difference in thermal expansion coefficient or strain due to bonding should be considered.

4.5 Finite Element Analysis of a Side-Cooled Diamond

To evaluate the performance of a side-cooled diamond monochromator under the heat load from the APS Undulator-A beam, a three-dimensional model was developed using the ANSYS[33] finite element analysis code.

The modeled geometry and crystal dimensions are shown in Fig. 4.2. The cooling of the monochromator is achieved by flowing water through four 6-mm-diameter circular channels located symmetrically relative to the crystal plane. Because of symmetry, only 1/4 of the monochromator was modeled. To define the worst-case scenario, one has to look at many different parameters, such as the absorbed power, the relative size of the footprint to the crystal size (see Eqn. 4.5), and finally the absorbed peak power density. The relevant quantity used for comparison of the results is the ratio of the thermally induced slope error to the Darwin width (σ_{max}/w_D).

In these FEA analyses, we choose to model a 0.3-mm-thick diamond crystal (with (111) orientation), which is about the thickness of the crystal we have at the APS. The analyses were performed for the first harmonics at 6 keV (Bragg angle=30.126°), and 4 keV (Bragg angle=48.826°), which correspond to the maximum absorbed power and to the largest absorbed peak power density and the smallest beam footprint, respectively. The FEA calculations showed that these two cases are comparable. They lead approximately to the same ratio σ_{max}/w_D. Therefore, only the 6 keV case is detailed here. For comparison, results of the 4 keV case are also given in Table 4.2. At the ring energy of 7 GeV and a current of 100 mA, Undulator A will radiate a total power of about 2.1 kW for the first harmonic at 6 keV (K=1.6). The normal incidence peak heat flux at 30 m from source, the monochromator location, is about 103 W/mm^2. Slits 3.6 mm vertical by 1.5 mm horizontal were used to allow most of the central cone of radiation to pass and impinge onto the crystal. This reduces the incident power to about 489 watts. The crystal (0.3 mm thick) absorbs about 92 watts of this power. The absorbed power was computed, using the UA code,[30] by dividing the crystal into four layers of equal thickness and calculating the power profile absorbed by each layer. A heat transfer coefficient of 1 W/cm^2-K was applied to the surfaces of the channels. The diamond thermal conductivity and coefficient of thermal expansion are taken from ref. 17. Variable material properties as a function of temperature are considered in the analysis.

For simplicity, the GaIn layer was omitted in the thermal finite element analysis, and, instead, an ideal contact was assumed between the crystal and the copper heat sink. The GaIn layer will certainly produce some resistance to the heat flow, which will result in some temperature
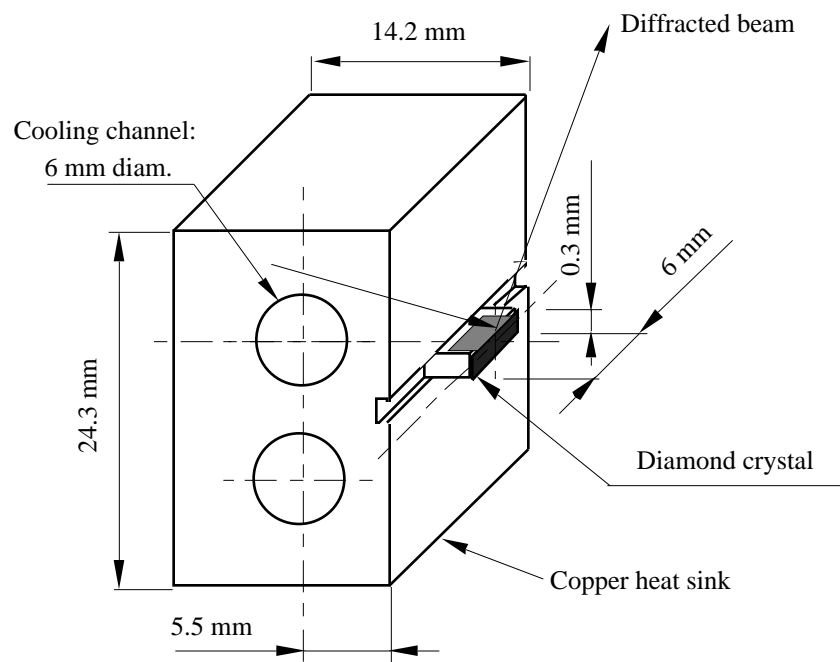
Figure 4.2. A perspective view of the geometry of the diamond modeled by the finite element analyses calculations. The crystal is cooled at the sides via a water-cooled copper heat sink with four circular channels located symmetrically relative to the crystal midplane. (Note that in the actual design the two copper blocks should be connected together to form a rigid structure and a clearance should be provided for the transmitted x-ray beam.)

drop across the interface. Consequently, the crystal temperature will be offset by roughly the same amount. The temperature drop across the crystal will remain the same because it depends primarily on the thermal conductivity of the diamond. Fortunately the thermal conductivity of diamond does not drop dramatically with temperature in the range of interest here. Therefore, if the temperature drop in the GaIn layer is not too large, the increase in the crystal distortion will be minimal.

Figure 4.3 shows the temperature contours in the crystal. A maximum temperature drop of 9.0°C is obtained across the crystal surface in the tangential direction and about 15.6°C in the sagittal direction. The peak temperature is about 48°C (at the center of the crystal), and the minimum temperature is 24.3°C (the coolant temperature was set to 20°C).

To compute the distortions, the crystal was held at one point at the center and its edges are left free. Because of the excellent thermal conductivity of diamond, the temperature drop across the crystal thickness is relatively small (= about 0.120°C). This gives a very small bending component, as expected. Therefore, the overall crystal distortions are mainly due to the temperature gradient across the crystal surface. Figure 4.4 shows the maximum displacement and slope error profiles on the crystal surface in the tangential and sagittal directions. A maximum tangential slope error of 1 arcsec (twice the value of the peak slope error) was obtained, which is much lower than the Darwin width of 7.0 arc seconds for 6 keV and symmetric (111) reflection. The slope error in the sagittal direction is about 1 arc second. Similar calculations were performed by the SPring-8 group.[35] A distortion angle of 0.5 arc seconds was obtained for a power and power density of 46 watts and 10 watts/mm^2, respectively, and the FEA calculations were in good agreement with the analytical model of a circular plate. In Table 4.2, we compare the results of the 6 keV and 4 keV cases. We see from this table that these cases are comparable. However, as mentioned previously, these calculations do not include the GaIn layer contribution. The temperature across the GaIn layer depends on the absorbed power for a fixed contact area. The absorbed power at 6 keV is about 18% higher than at 4 keV (92 watts versus 78 watts) therefore the 6 keV case will give the higher ratio $_{max}/w_D$.

In summary, the cases studied here (the geometries for 6 and 4 keV photons) correspond to the worst-case scenarios. The FEA results show that both cases are comparable. The thermally induced slope errors are much smaller than the Darwin widths for the corresponding energies. In this model, we have omitted the effect the GaIn layer because we believe that the temperature across the joint diamond heat sink can be minimized by optimizing the size of the contact area (see Section 4.4). Because of smaller Bragg angles, the absorbed power is much higher for the higher harmonic energies. However in this case, one can simply use filters to cut off the unwanted radiation from lower energy photons, thereby reducing significantly the power load on the crystal. Therefore we conclude from this analyses that a diamond crystal is a good option as a monochromator for the APS Undulator A.

4.6 Effect of the Vertical Slits

As mentioned previously, the temperature drop across the crystal thickness is relatively small, and the slope error on the crystal surface is essentially due to the variation of the temperature on the crystal surface, which is introduced by the sharp cut of the heat flux by the slits. It has been shown[12] that, for side-cooled thin diamond crystals, if the vertical slit opening is wider that the crystal size (see Figure 4.5), the temperature profile in the tangential direction becomes almost flat, thereby reducing the slope error to a minimum under the useful beam. This, of course, will result in a slight increase of the sagittal slope error due to the increase in the absorbed power compared to a smaller beam and same crystal size. However, considering the good thermal (and absorption) properties of diamond combined with the small size of the crystal, the extra power absorbed by diamond will have only a small effect.

Table 4.2. Summary of thermal and distortion results for 6 and 4 keV cases. These results are for Undulator A beam at 7 GeV 100 mA operation with 1.5 mm x 3.6 mm slit opening at 30 from the source, the monochromator location. No filters or windows are considered here. E_1 is the energy of the first harmonic, P is the absorbed power, Pd is the absorbed peak power density, T_{max} is the temperature at the center of the crystal, T_{Tang} and $_{Tang}$ are, respectively, the temperature drop and the slope error across the crystal surface in the tangential direction, T_{sag} and $_{Sag}$ are, respectively, the temperature drop and the slope error across the crystal surface in the sagittal direction. The symmetric (111) diamond Darwin width, w_D, is equal to about 7.0 arsec at 6 keV and 13.9 arcsec at 4 keV.

E_1 (keV)	θ_{Bragg} (deg.)	P (watts)	Pd (W/mm^2)	T_{max} (°C)	ΔT_{Tang} (°C)	ΔT_{sag} (°C)	Tang (arsec.)	Sag (arsec.)	$_{max}/w_D$
4.0	48.826	78.0	10.9	65.0	11.85	25.2	2.0	3.2	0.138
6.0	30.126	92.0	10.3	48.0	9.1	15.6	1.0	1.3	0.137
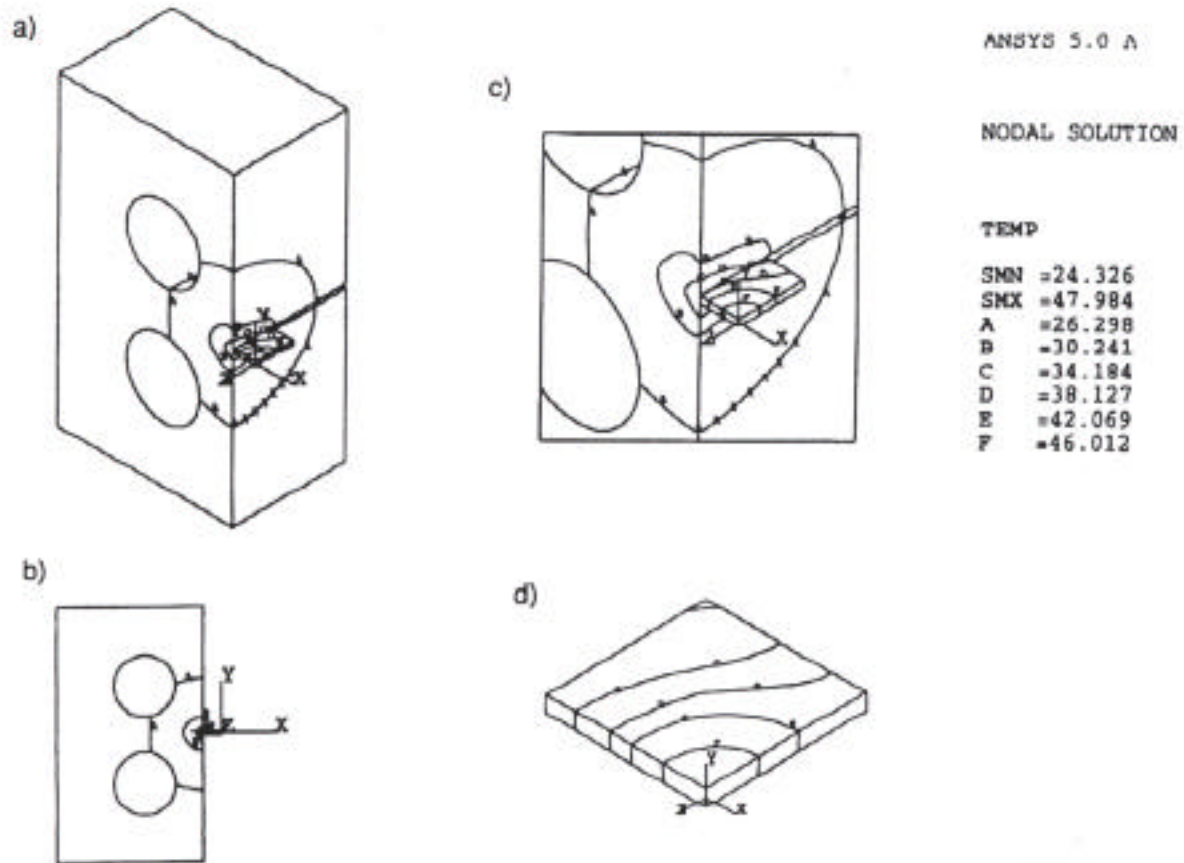
Figure 4.3. Temperature contours of a diamond crystal under Undulator A beam at 7 GeV and 100 mA. The figure shows (a) 1/4 of the entire structure crystal-heat-sink, (b) one half of the end view (at reduced scale, (c) a close-up view around the crystal, and (d) a perspective view of 1/4 of the crystal alone. The values of the isotherms are indicated with letters, SMX amd SMN are the maximum and minimum temperatures, respectively. The crystal was assumed to have (111) orientation and was set to diffract the first harmonic at 6 keV (K=1.644, Bragg angle=30.126°). A heat transfer coefficient of 1 W/cm^2 was applied to the surface of the channels. The GaIn layer was not included in this model, and, instead an ideal contact (i.e., no contact thermal resistance) was assumed between the crystal and the heat sink.

a)
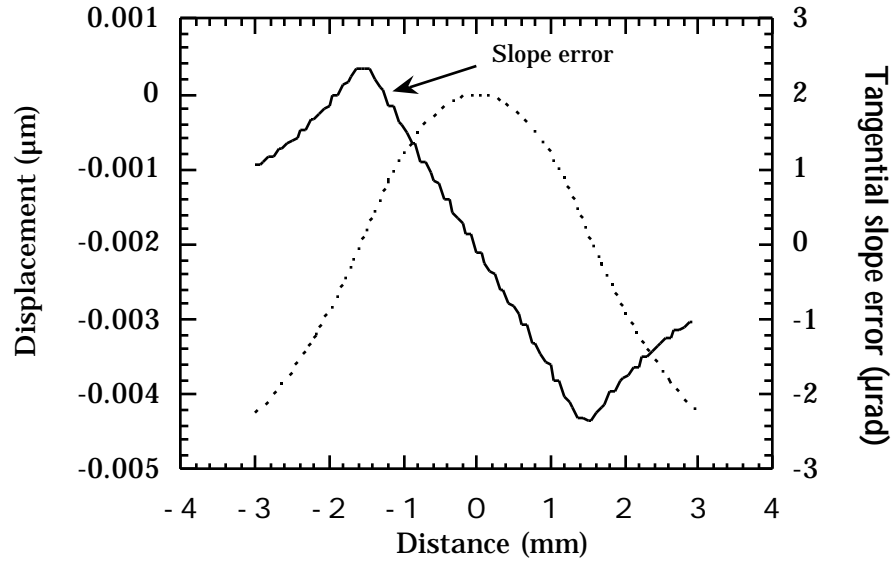
b)
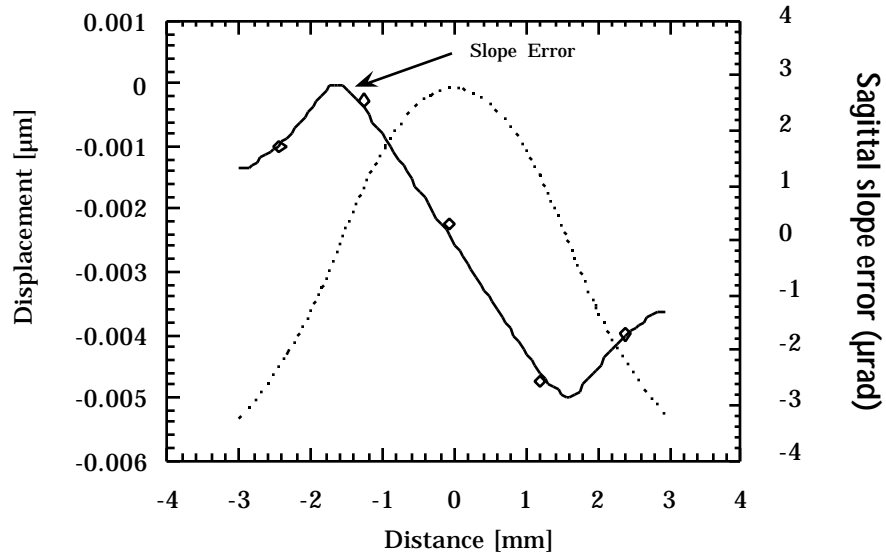
Figure 4.4. Displacement and slope error profiles along the crystal's axis in the (a) tangential and (b) sagittal directions, on the surface of a diamond crystal under Undulator A beam at a ring energy of 7 GeV and a current of 100 mA. The crystal (0.3 mm thick) has (111) orientation and was set to diffract the first harmonic at 6 keV (k=1.644, Bragg angle=30.126°). No filters or windows were considered in the calculations. (The "stairs" on the curves are due to numerical error.)
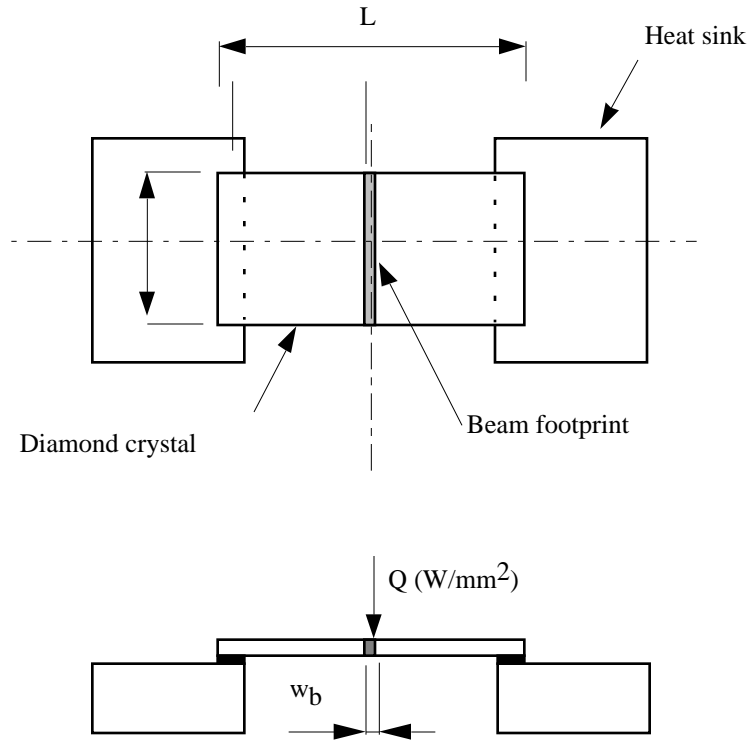
Figure 4.5. A side-cooled thin crystal with the vertical slit opening wider than the crystal dimension will avoid the sharp temperature gradient along the beam direction, thereby reducing the slope error (in this direction) to a minimum. This, of course, will result in a slight increase of the sagittal slope error compared with a smaller beam and the same crystal size.

5. SUMMARY AND APS RESEARCH PLANS

No attempt is made in this report to produce a list of "pros" and "cons" on the use of diamonds as high-heat-load monochromators, although such information is dispersed throughout the text. The reason for this is that it is difficult to generically weigh each of the advantages or disadvantages - that is too dependent on the requirements of the particular science to be performed at the beamlines. The purpose of this manuscript is to provide the researcher with some basic properties of diamonds (and a set of references). In addition we have tried to highlight some of the principal differences in the use of diamonds for monochromators as compared to silicon, a familiar monochromator material, and where appropriate to point out some of the problems associated with the use of diamonds that as of yet do not have completely satisfactory solutions.

There is no doubt that the thermal and mechanical properties of diamonds make it an ideal candidate for high heat flux x-ray monochromators. Although the current difficulties in the procurement of high-quality single-crystal diamonds may be considered an impediment to their routine use, perhaps the primary factor that must be considered when choosing diamonds as monochromating crystals is whether the loss of a factor of two in the flux when using diamond (as compared with Si (111)) is acceptable for a particular scientific program. In some instances, this loss of flux can be compensated for by the potential of using the transmitted beam through the diamond monochromator for other experiments, as has been proposed by the Troika beamline at the ESRF. This is only one example of the many variables that need to be weighed in the decision making process.

Diamonds with the (400) planes parallel to the large surface are more readily available. Unfortunately, the loss of flux when using (400) diamonds crystals is simply too large to tolerate, and, therefore for a majority of applications, [400] oriented platelets should be considered un-acceptable as monochromating crystals. The [400] plates can be oriented to diffract x-rays from the asymmetrical (111) planes in a Laue geometry, however the reduction of flux from the Laue geometry and the narrower energy bandwidth cannot be compensated for by the asymmetrical aspect of the reflection over any appreciable energy range.

Good quality diamonds of the required size (8mm x8mm is probably the required to have adequate surface area available to remove the deposited heat from the APS undulator beam) are difficult to obtain in a consistent fashion.

Procedures for assuring strain-free mounting while maintaining good thermal contact with the cooled substrate is an area where more work needs to be done. The use of the surface tension of liquid metals to perform this task may be adequate, however other approaches need to be explored.

To summarize, our current program on the use of diamonds for high-heat-load monochromator has lead us to investigate the following areas:

(i)   development of sources of good diffraction diamonds
(ii)   measurements of the boundary heat transfer conductance between
        Cu/GaIn/diamond
(iii)   HHL testing of those diamonds we now have in hand
(iv)   FEA and analytical modeling of diamonds subjected to HHL synchrotron beams
(v)   methods of attachment of diamonds to substrates

6. ACKNOWLEDGMENTS

7. REFERENCES

1.	S. Sharma, L. E. Berman, J. B. Hastings, and M. Hart, "Adaptive Optics for High Power Beamlines Using Diamond Crystal Monochromators," SPIE **1739**: *High Heat Flux Engineering*, 604 - 614, 1992.

2.	J. D. Stephenson, "A Choice of Diamond Single Crystals for First SR-(Undulator-) Monochromators," Phys. Stat. Sol **A134**, p 373, 1992.

3.	A. M. Khounsary, R. K. Smither, and S. Davey, "Diamond Monochromator for High Heat Flux Synchrotron X-ray Beams," SPIE **1739**: *High Heat Flux Engineering*, p629, 1992.

4.	A. K. Freund, "Experience with Diamond Monochromators," Thermal Management of X-ray Optical Components for Synchrotron Radiation Workshop at Argonne National Laboratory, as part of The International Conference on Synchrotron Radiation Instrumentation, Stony Brook NY, USA (1994); "Diamond Single Crystals: The Ultimate Monochromator Material for High Power X-Ray Beams," Opt. Eng., 3**4,** 432-440, 1995.

5	L. E. Berman, J. B. Hastings, D. P. Siddons, M. Koike, V. Stojanoff, and M. Hart, "Diamond Crystal X-ray Optics for High-Power-Density Synchrotron Radiation Beams," Nuc. Inst. Meths. Phys. Res. **A 329**, p 555-563 (1993). The authors' estimate of the highest power FWHM (19.9 µrad) based upon the change in the peak amplitude of the rocking curve has been replaced in Table 1.1 with the FWHM (27.5 µrad) as measured from the authors' Fig. 4.

6.	L. E. Berman and M. Hart, "Preserving the High Finesse of X-ray Undulator Beams from Perfect Water-Jet-Cooled Diamond Monochromators," Nucl. Instrum. Methods **A334**, 617-620 (1993).

7.	J. Als-Neilsen, A. K. Freund, and G. Grubel, "Diamond Crystal Monochromator Performance under Full Load from ESRF Undulator," ESRF Newsletter **16**, 9-10 (Jan., 1993).

8.	T. Ishikawa, private communications.

9.	In order to achieve the expected total power and peak power density of an APS or SPring-8 beam it is necessary to doubly focus one of the existing high power wiggler beams. This necessarily produces a strongly convergent beam incident on the first crystal (located at the focus) and therefore a strongly divergent beam at the second crystal. This severely limits the information that can be obtained on the beam walk and beam spreading due to thermal and mounting distortions. Typically, only the beam throughput is measured.

10.	R. C. Blasdell, A. T. Macrander, and W. K. Lee, "A Ray-Tracing Study of Inclined Double-Crystal Monochromators," Nucl. Instrum. Methods **A347**, 327-330 (1994).

11.	A. K. Freund, "Recent Results of High Heat Load Crystal Optics Experiments at the ESRF," SPIE **1997**: *High Heat Load Engineering II,* 208-222 (1993).

12.	L. Assoufid and D. M. Mills, "Thermal and Structural Analysis for a Diamond Monochromator Subjected to the APS Undulator A X-ray Beam," presented at the Workshop on the Thermal Management of X-ray Optical Components for Synchrotron Radiation, July 14-15, 1994, Argonne National laboratory.

13. J. Wilks and E. Wilks, *Properties and Applications of Diamond*, Butterworth-Heinemann Ltd., Boston (1991).

14. J. E. Field ed., *The Properties of Diamond*, Academic Press Limited, New York (1979).

15. W. Kaiser and W. L. Bond,"Nitrogen, A Major Impurity in Common Type I Diamond," Phys. Rev. **115**, 857 (1959).

16. H. Holloway, K. C. Hass, M. A. Tamor, T. R. Anthony, and W. F. Banholzer, "Isotopic Dependence of the Lattice Constant of Diamond," Phys. Rev. **B44**, 7123 (1991).

17. Y.S. Touloukian, R.W. Powell, C.Y. Ho and P.G. Klemens, *Thermophysical Properties of Matter*, Vols. 2 and 13, IFI/Plenum, New York (1970).

18. J. W. Vandersande, "Thermal Conductivity of Natural-Isotope Diamond," pp. 33-35 in *Properties and Growth of Diamond*, G. Davies, ed., INSPEC, London (1994).

19. K. Haruna and H. Maeta, "Thermal Expansion of Synthetic Diamond Single Crystals at Low Temperatures," Diamond and Related Materials **2**, 859-861 (1993).

20. H. J. McSkimin and P. Andreatch, Jr., "Elastic Moduli of Diamond as a Function of Pressure and Temperature," J. Appl. Phys. **43(7)**, 2944-2948 (1972).

21. U. Schumacher and R. Nolte, "Local Crystal Lattice Curvature Measurements for Bent-Crystal Spectrometers," Rev. Sci. Instrum. **61**, 121 (1990).

22. R. K. Smither, G. A. Forster, D. H. Bilderback, M. Bedzyk, K. Finkelstein, C. Henderson, J. White, L. E. Berman, P. Stefan, and T. Oversluizen, "Liquid Gallium Cooling of Silicon Crystals in High Intensity Photon Beams," Rev. Sci. Instrum. **60**, 1486-1492 (1989).

23. J. Als-Nielsen, A. K. Freund, M. Wulff, M. Hanfland, and D. Hausermann, "Performance of Diamond as X-ray Monochromator under Very High Heat Flux in a Synchrotron Beam," Nuc, Inst. Methods **B94**, 348-350, 1994.

24. M. Hart, Notes from the Inter-CAT Technical Working Group: September 19, 1994.

25. The diamond was cleaned between the second and third measurements in order to test whether the apparent pits were real. It is also possible that water or some other fluid accumulated in the pits but was not completely removed, resulting in the disappearance of the pits in the third set of optical measurements. In this case, the prior two measurements of the etch rate (which agree) might be correct.

26. B. W. Batterman and H. Cole, "Dynamical Diffraction of X-rays by Perfect Crystals," Rev. Mod. Phys **36**, 681-717 (1964).

27. W. H. Zachariasen, *Theory of X-ray Diffraction in Crystals,* John Wiley & Sons, Inc., New York (1945).

28. T. Hon, W. Kiszenick, and B. Post, "Accurate Lattice Constants from Multiple Reflection Measurements II. Lattice Constants of Germanium, Silicon, and Diamond," J. Appl. Cryst. **8**, 457-458, 1975.

29.   Richard Deslattes and Albert Henins, "X-ray to Visible Wavelength Ratios," Phys. Rev. Letts, **31**, 972-975, 1973.

30.   R. Dejus, ANL, unpublished information, 1994.

31.   Jens Als-Nielsen, A. K. Freund, G. Grubel, J. Linderholm, M. Nielsen, M. Sanchez del Rio, J.P.F. Sellschop, "Multiple Station Beamline at an Undulator X-ray Source," Nucl. Instrum. Methods B **94**, 306, 1994.

32.   See for example *A Guide to Neutron Research Facilities at the ILL*, Herma Blank and Bernd Mair, eds., Institut Max von Laue - Paul Langevin, Grenoble France, 1988 or other descriptions of ILL beamline layouts.

33.   ANSYS-A general purpose finite element analysis program, Rev. 5.0.a, Swanson Analysis System, Inc., Houston, PA 15342, USA.

34.   H. Yamaoka, A.K. Freund, J. Holmberg, M. Rossat, M. Wulff, M. Hanfland, W-K. Lee, D. M. Mills, and S. Rogers, "Experience from a Cryogenically Cooled Diamond Crystal Monochromator," submitted for publication to Nuclear Instruments and Methods.

35.   Hitoshi Yamaoka, Kiyotaka Ohtomo, and Tetsuya Ishikawa, "Diamond Crystal Monochromator in a SPring-8 Undulator Beamline," Rev. Sci. Instrum. **66**, 2116-2118, 1995.

Appendix A: Thermal Properties of Diamond

Table A1 gives suggested values of the thermal conductivity, k, of type I, IIa, and IIb diamond with the natural isotope concentration (98.93% ^{12}C, 1.07% ^{13}C) as a function of temperature, T.[17] Columns 2, 3, and 7 are suggested literature average values from 1970.[17] Columns 3, 5, and 6 are from a 1994 reveiw of recent experimental data.[18]

Table A2 gives suggested values of the thermal expansion coefficient.

Table A1. Suggested values of the thermal conductivity of diamond.

T	k [W/cm-K]					
[K]	Type I	Several Ia	Type IIa	Best IIa	Isotop. pure	Type IIb
10.0	1.42	1 - 2	3.24	2.0		2.07
11.0	1.82		4.09			2.63
12.0	2.28		5.10			3.29
13.0	2.81		6.20			4.02
14.0	3.39		7.45			4.87
15.0	4.03		8.77			5.77
16.0	4.72		10.2			6.75
18.0	6.27		13.5			8.90
20.0	8.00		17.1			11.4
25.0	13.1		27.4			18.5
30.0	19.0		39.5			26.9
35.0	24.9		52.5			35.6
40.0	29.7		66.7			44.6
45.0	33.2		80.2			53.0
50.0	35.6		93.0			59.6
60.0	37.5		113.0			68.0
70.0	37.1		120.0			69.1
80.0	35.3		117.0			65.9
90.0	32.8		110.0			60.3
100.0	30.1	12 - 52	100.0	125	-	54.5
150.0	19.5		60.5			32.6
200.0	14.2	10 - 30	40.4	55	75	22.6
250.0	11.1		29.7			17.1
273.2	10.0		26.3			15.3
300.0	9.00	5 - 18	23.1	25	32	13.5
350.0	7.58		18.6			11.2
400.0	6.52		15.5			9.36
450.0	-	4 - 12	-	13	18	-

Table A2. Suggested values of the linear thermal expansion, $\Delta L/L_{293K}$, and the linear thermal expansion coefficient, α, of diamond.[17] The thermal expansion is claimed to be accurate to $\pm 7\%$. The low temperature values of α are therefore of marginal significance.[19]

T (K)	$\Delta L/L_{293K}$ (10^{-2})	α (10^{-6} /K)
25	-0.011	-0.1
50	-0.012	-0.06
100	-0.012	0.05
150	-0.011	0.2
200	-0.009	0.4
250	-0.005	0.7
293	0.000	1.0
350	0.008	1.5
400	0.016	1.8
500	0.037	2.3
600	0.062	2.8
700	0.093	3.2
800	0.127	3.7
900	0.166	4.0

Appendix B: Structure Factors, Widths, and Reflectivities

Calculations were done using the MAKE_PCSF program, which is a heavily modified version of the SHADOW program BRAGG. Unmodified atomic scattering factors are experimental values from the literature, Honl corrections are from the SHADOW code's internal tables. The Darwin width cited is a form that incorporates absorption and so will be slightly different than the zero absorption result usually given. The reflectivity curves are integrated numerically and so the range and step sizes are given. The errors will be largely dominated by the uncertainty in f_O, the Debye Waller amplitude factor (DWAF), and the Honl corrections and may amount to a percent or two in the value of the structure factor and as much as a percent or two in the results. The numerical integrations should be more accurate though this was not tested.

Diamond (111)

T = 298.15 K
a = 3.567140 Å.
d = 2.059489 Å.
q_X-ray = 0.2427787 1/Å.
fo = 3.305
DWAF = 0.9883

Energy (keV)	4.000	6.000	8.000	10.000	15.000	20.000
f' (electrons/atom)	0.062	0.032	0.019	0.012	0.001	-0.004
f'' (electrons/atom)	0.043	0.018	0.010	0.006	0.002	0.001
Kinematic Bragg Angle (deg.)	48.809487	30.111385	22.102332	17.518251	11.576320	8.656181
Dynamical Bragg Angle (deg.)	48.814810	30.114073	22.104211	17.519709	11.577265	8.656883
Darwin Width (μrad)	72.14	36.28	25.30	19.63	12.69	9.42
R_max	0.974	0.989	0.994	0.996	0.999	0.999
Delta theta (±μrad)	300	150	100	80	60	40
dTheta (μrad)	1.00	0.50	0.25	0.20	0.20	0.10
FWHM R(theta) (μrad)	76.78	38.58	26.87	20.83	13.49	9.99
Integral R(theta) (μrad)	90.16	46.41	32.60	25.42	16.53	12.27
FWHM R^2(theta) (μrad)	73.00	36.85	25.74	19.96	12.94	9.58
Integral R^2(theta) (μrad)	69.66	37.03	26.33	20.65	13.43	10.03
Delta E (±eV)	1.2	1.5	2.0	3.0	4.0	5.0
dE (eV)	0.004	0.005	0.005	0.010	0.010	0.010
FWHM R(E) (eV)	0.2688	0.3988	0.5292	0.6598	0.9866	1.3131
Integral R(E) (eV)	0.3164	0.4795	0.6424	0.8087	1.2089	1.6094
FWHM R^2(E) (eV)	0.2552	0.3811	0.5071	0.6550	0.9450	1.2576
Integral R^2(E) (eV)	0.2437	0.3828	0.5188	0.6354	0.9852	1.3158

Si (1 1 1)

T = 298.15 K
a = 5.431054 Å
d = 3.135620 Å
q_X-ray = 0.1594581 1/Å
fo = 10.782
DWAF = 0.9884

Energy (keV)	4.000	6.000	8.000	10.000	15.000	20.000
f' (electrons/atom)	0.400	0.344	0.256	0.194	0.090	0.043
f'' (electrons/atom)	1.191	0.567	0.329	0.214	0.096	0.053
Kinematic Bragg Angle (deg.)	29.621033	19.238876	14.307775	11.402751	7.573790	5.673079
Dynamical Bragg Angle (deg.)	29.625202	19.241408	14.309612	11.404196	7.574735	5.673783
Darwin Width (μrad)	29.63	47.70	34.52	27.13	17.71	13.17
R_max	0.805	0.901	0.941	0.961	0.982	0.990
Delta theta (±μrad)	300	100	100	100	80	40
dTheta (μrad)	1.00	0.50	0.50	0.25	0.20	0.10
FWHM R(theta) (μrad)	80.18	50.28	36.66	28.85	18.82	13.99
Integral R(theta) (μrad)	75.77	51.79	40.47	33.09	22.45	16.73
FWHM R^2(theta) (μrad)	66.17	45.27	34.14	27.22	17.94	13.37
Integral R^2(theta) (μrad)	42.13	35.46	29.51	24.93	17.60	13.49
Delta E (±eV)	2	2	4	4	8	10
dE (eV)	0.01	0.01	0.01	0.01	0.02	0.03
FWHM R(E) (eV)	0.5642	0.8643	1.1494	1.4302	2.1233	2.8175
Integral R(E) (eV)	0.5320	0.8973	1.2798	1.6293	2.5250	3.3903
FWHM R^2(E) (eV)	0.4657	0.7780	1.0699	1.3494	2.0259	2.6933
Integral R^2(E) (eV)	0.2963	0.6096	0.9256	1.2359	1.9854	2.7175

Ge (111)

T = 298.15 K
a = 5.657820 Å
d = 3.266544 Å.
q_X-ray = 0.153067 1/Å
fo = 27.908
DWAF = 0.9868

Energy (keV)	4.000	6.000	8.000	10.000	15.000	20.000
f' (electrons/atom)	0.072			-2.098		
f'' (electrons/atom)	3.098			0.622		
Kinematic Bragg Angle (deg.)	28.323610			10.939969		
Dynamical Bragg Angle (deg.)	28.332075			10.942770		
Darwin Width (μrad)	180.14			58.90		
R_max	0.798			0.952		
Delta theta ($\pm \mu$rad)	700			200		
dTheta (μrad)	2.00			0.50		
FWHM R(theta) (μrad)	182.76			62.58		
Integral R(theta) (μrad)	171.66			70.64		
FWHM R^2(theta) (μrad)	150.05			58.69		
Integral R^2(theta) (μrad)	94.23			52.39		
Delta E ($\pm$eV)	5			12		
dE (eV)	0.02			0.03		
FWHM R(E) (eV)	1.3560			3.2376		
Integral R(E) (eV)	1.2719			3.6694		
FWHM R^2(E) (eV)	1.1136			3.0372		
Integral R^2(E) (eV)	0.6990			2.7096		

R_max	maximum value of reflectivity curve
Delta theta	range of integration over angle
dTheta	step size for angle integration
FWHM R(theta)	full width at half maximum of the reflectivity vs. angle curve
Integral R(theta)	integral of the reflectivity vs. angle curve
FWHM R^2(theta)	full width at half maximum of the square of the reflectivity vs. angle curve
Integral R^2(theta)	integral of the square of the reflectivity vs. angle curve
Delta E	range of integration over energy
dE	step size for energy integration
FWHM R(E)	full width at half maximum of the reflectivity vs. energy curve
Integral R(E)	integral of the reflectivity vs. energy curve
FWHM R^2(E)	full width at half maximum of the square of the reflectivity vs. energy curve
Integral R^2(E)	integral of the square of the reflectivity vs. energy curve

Appendix C: Results of Absorption Calculations

Table C1. Absorbed power for the first harmonic energies, symmetric diamond (111) Bragg geometry.

E_1[keV]	Absorbed power [watts]		
	t=0.1 mm	t=0.3 mm	t=0.5 mm
4.0000	46.94	78.390	98.580
5.0000	50.08	87.632	109.43
6.0000	49.30	91.948	114.69
7.0000	45.96	91.164	114.73
8.0000	41.028	85.788	109.62
9.0000	35.153	76.712	99.768
10.000	28.752	64.904	85.850
11.000	21.460	49.892	67.144
12.000	15.047	35.643	48.536

Table C2. Absorbed power for the third harmonic energies, symmetric diamond (111) Bragg geometry.

E_3[keV]	Absorbed power [watts]		
	t=0.1 mm	t=0.3 mm	t=0.5 mm
12.000	78.388	127.28	157.22
13.000	81.996	132.74	163.56
14.000	85.076	137.19	168.75
15.000	87.632	140.67	172.78
16.000	89.648	143.26	175.68
17.000	91.084	144.96	177.48
18.000	91.948	145.87	178.09
19.000	92.236	146.05	177.76
20.000	91.968	145.56	176.52

Table C3. Absorbed peak surface power density for the first harmonic energies, symmetric diamond (111) Bragg geometry.

E_1[keV]	Absorbed power [watts]		
	t=0.1 mm	t=0.3 mm	t=0.5 mm
4.0000	7.3978	11.464	14.000
5.0000	6.6179	11.002	13.206
6.0000	5.6203	10.227	12.325
7.0000	4.6152	9.1228	11.230
8.0000	3.6939	7.8056	9.8830
9.0000	2.8771	6.4032	8.3436
10.000	2.1784	5.0101	6.6962
11.000	1.5109	3.5938	4.9185
12.000	0.9855	2.4027	3.3370

Table C4. Absorbed peak surface power density for the third harmonic energies, symmetric diamond (111) Bragg geometry.

E_3[keV]	Absorbed power [watts]		
	t=0.1 mm	t=0.3 mm	t=0.5 mm
12.000	3.8192	5.9258	7.3189
13.000	3.7781	5.7743	7.0825
14.000	3.7281	5.6229	6.8529
15.000	3.6669	5.4714	6.6408
16.000	3.5953	5.3216	6.4168
17.000	3.5082	5.1664	6.1908
18.000	3.4088	5.0109	5.9700
19.000	3.2966	4.8529	5.7485
20.000	3.1731	4.6924	5.5263

Table C5. Absorbed power and power density for the first harmonic energies in the Laue geometry. E_1 is the energy of the first harmonic, t_{eff} is the effective thickness ($= t / \cos(\theta_{Bragg})$), P_d is the absorbed power density, and P is the absorbed power.

E_1 (keV)	θ_{Bragg} (deg.)	t_{eff} (mm)	P_d (W/mm^2)	P (watts)
4.0000	48.826	0.15190	6.89	50.30
5.0000	37.026	0.12526	7.34	41.70
6.0000	30.120	0.11561	6.47	32.90
7.0000	25.475	0.11077	5.35	25.20
8.0000	22.108	0.10794	4.27	19.00
9.0000	19.545	0.10611	3.30	14.10
19.000	17.523	0.10487	2.46	10.20
11.000	15.885	0.10397	1.69	6.80
12.000	14.531	0.10330	1.10	4.30

Table C6. Absorbed power and power density for the third harmonic energies on the Laue geometry. E_3 is the energy of the first harmonic, t_{eff} is the effective thickness ($= t / \cos(\theta_{Bragg})$), P_d is the absorbed power density, and P is the absorbed power.

E_3 (keV)	θ_{Bragg} (deg.)	t_{eff} (mm)	P_d (W/mm^2)	P (watts)
12.000	14.531	0.10330	8.36	40.900
13.000	13.392	0.10279	8.31	39.800
14.000	12.419	0.10240	8.10	38.100
15.000	11.579	0.10208	7.81	36.200
16.000	10.847	0.10182	7.44	34.000
17.000	10.201	0.10161	7.05	31.800
18.000	9.6291	0.10143	6.65	29.600
19.000	9.1179	0.10128	6.24	27.400
20.000	8.6584	0.10115	5.83	25.300